



PCCP

The Influence of Model Building Schemes and Molecular Dynamics Sampling on QM-cluster Models: The Chorismate Mutase Case Study

Journal:	<i>Physical Chemistry Chemical Physics</i>
Manuscript ID	CP-ART-12-2023-006100.R2
Article Type:	Paper
Date Submitted by the Author:	21-Mar-2024
Complete List of Authors:	Agbaglo, Donatus; The University of Memphis,, Chemistry Summers, Thomas; The University of Memphis, Department of Chemistry Cheng, Qianyi; The University of Memphis,, Department of Chemistry DeYonker, Nathan; The University of Memphis,, Chemistry

SCHOLARONE™
Manuscripts

The Influence of Model Building Schemes and Molecular Dynamics Sampling on QM-cluster Models: The Chorismate Mutase Case Study

Donatus A. Agbaglo,[†] Thomas J. Summers,^{†,‡} Qianyi Cheng,[†] and Nathan J. DeYonker^{*,†}

[†]*Department of Chemistry, University of Memphis, Memphis, TN 38152, U.S.A.*

[‡]*Theoretical Division, Los Alamos National Laboratory, Los Alamos, NM 87545, U.S.A.*

E-mail: ndyonker@memphis.edu

1 Abstract

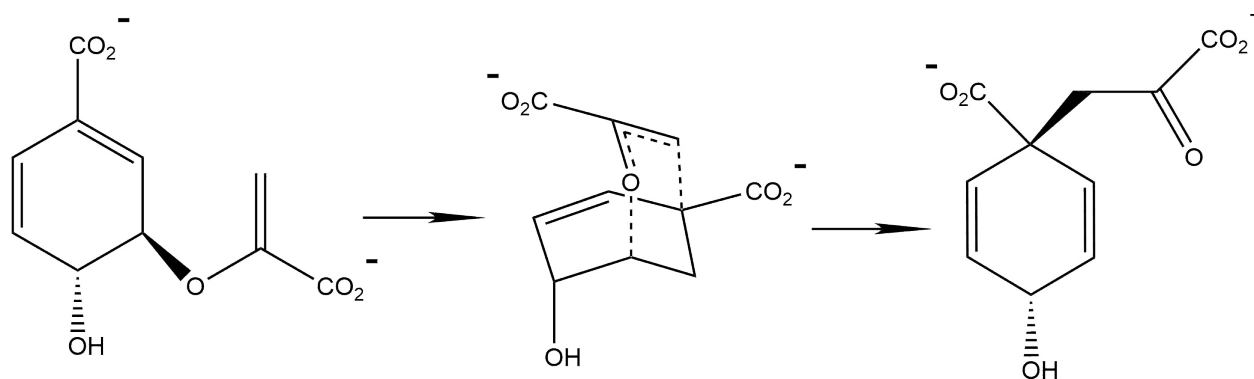
2 Most QM-cluster models of enzymes are constructed based on X-ray crystal structures, which
3 limits comparison to *in vivo* structure and mechanism. The active site of chorismate mutase
4 from *Bacillus subtilis* and the enzymatic transformation of chorismate to prephenate is used
5 as a case study to guide construction of QM-cluster models built first from the X-ray crystal
6 structure, then from molecular dynamics (MD) simulation snapshots. The Residue Interac-
7 tion Network-based ResidUe Selector (*RINRUS*) software toolkit, developed by our group to
8 simplify and automate the construction of QM-cluster models, is expanded to handle MD to
9 QM-cluster model workflows. Several options, some employing novel topological clustering
10 from Residue Interaction Network (RIN) information, are evaluated for generating conforma-
11 tional clustering from MD simulation. *RINRUS* then generates a statistical thermodynamic
12 framework for QM-cluster modeling of the chorismate mutase mechanism via refining 250

13 MD frames with Density Functional Theory (DFT). The 250 QM-cluster models sampled
14 provide a mean ΔG^\ddagger of 10.3 ± 2.6 kcal mol⁻¹ compared to the experimental value of 15.4
15 kcal mol⁻¹ at 25 °C. While the difference between theory and experiment is consequential,
16 the level of theory used is modest and therefore “chemical” accuracy is unexpected. More
17 important are the comparisons made between QM-cluster models designed from the X-ray
18 crystal structure versus those from MD frames. The large variations in kinetic and ther-
19 modynamic properties arise from geometric changes in the ensemble of QM-cluster models,
20 rather from the composition of the QM-cluster models or from the active site-solvent inter-
21 face. The findings open the way for further quantitative and reproducible calibration in the
22 field of computational enzymology using the model construction framework afforded with
23 the *RINRUS* software toolkit.

24 Introduction

25 Through multiscale QM/MM or QM-only “cluster model” studies, stationary points along a
26 reaction mechanism can be optimized, which allows a structural probe of the enzyme kinet-
27 ics that is impossible to directly observe experimentally.¹ As the reliability of computational
28 enzymology and the tractable size of QM-regions increase, a greater focus on cyberinfrastruc-
29 ture is required for building consistent and reproducible atomic-level enzyme models. Our
30 group has developed the Residue Interaction Network Residue Selector (*RINRUS*) software
31 toolkit to facilitate studying the reaction mechanisms of enzymes with quantum chemistry.²⁻⁴
32 Instead of relying on chemical intuition or distance-based criteria to prioritize the critical
33 fragments within the enzyme active site, *RINRUS* algorithmically constructs enzyme models
34 based on several possible qualitative and quantitative criteria. *RINRUS* infrastructure was
35 first developed to build QM-cluster models of enzymes, but adapting the code to also build
36 QM/MM enzyme models is in progress. In this work, we explore the enzyme chorismate mu-
37 tase in conjunction with a proof-of-concept expansion of *RINRUS* capabilities: interfacing

38 QM-cluster modeling with Molecular Dynamics (MD) techniques.



Scheme 1: Schematic representation of the Claisen rearrangement of chorismate to prephenate

39 Chorismate mutase (CM) catalyzes the reaction of chorismate to prephenate, participat-
 40 ing in the shikimate pathway that biologically produces phenylalanine and tyrosine amino
 41 acids (Scheme 1).⁵⁻¹⁴ The shikimate pathway does not occur in the animal kingdom, and
 42 thus provides a target for the development of new antibiotics, fungicides, and herbicides.¹⁵
 43 While chorismate mutase has been widely studied experimentally and computationally, there
 44 are still mysteries to be unraveled with respect to the extraordinary kinetic enhancement of
 45 its active site. The chorismate mutase enzymatic reaction promotes a 10⁶-fold rate accelera-
 46 tion of prephenate production through a Claisen rearrangement in the catalytic elementary
 47 step.^{16,17} This Claisen rearrangement is one of the few known examples of a naturally-
 48 occurring catalyzed pericyclic reaction.¹⁸ In 1993, Lipscomb and coworkers published an
 49 X-ray crystal structure of *Bacillus subtilis* chorismate mutase (BsCM, PDB: 2CHT) at 2.2
 50 Å resolution that forms the basis of most theoretical works.¹⁹ This structure contains an
 51 endo-oxabicyclic transition state analogue (TSA), 8-hydroxy-2-oxa-bicyclo[3.3.1]non-6-ene-
 52 3,5-dicarboxylic acid, which offered structural insight into the enzyme mechanism. Since the
 53 pericyclic reaction does not involve covalent substrate-protein bonding or acid-base chem-
 54 istry, CM makes an intriguing, and in some respects, simplified case study of enzyme catal-
 55 ysis.^{20,21}

56 Mutagenesis, computational enzymology, and biochemical kinetics have been indispens-

57 able tools to study the mechanism of the CM reaction, especially for exploring the transition
58 state stabilization (TSS) and near-attack conformation (NAC) hypotheses or for describ-
59 ing manifestations of their complementary kinetic and thermodynamic behavior.^{9,18,22–25}
60 Mutagenesis experiments of *Escherichia coli* chorismate mutase (EcCM)^{26–30} and BsCM
61 revealed the catalytic importance of many charged active site residues for establishing hy-
62 drogen bonding with the negatively charged substrate. For example, replacement of Arg90
63 with a positively-charged lysine still decreases the catalytic efficiency by at least three orders
64 of magnitude in BsCM.^{19,31}

65 Theoretical studies of chorismate mutase with QM/MM-MD first emphasized the im-
66 portance of a near attack conformation (NAC) as the main catalytic driving power behind
67 the proposed mechanism.^{20,32,33} Studies done by Bruice and co-worker showed that NAC
68 rearrangement of chorismate structure is a result of activated carbon and oxygen ligand
69 atoms approaching within the van der Waals contact distance at very small bond angles,
70 creating a favorable orientation of π -orbital overlap.^{20,32} The proponents of the NAC hy-
71 pothesis focus on geometric distortion of the substrate in the active site. However, those
72 who argue for the TSS hypothesis indicate that positively charged residues like Lys39 in
73 EcCM and Arg90 in BsCM stabilize the developing negative charge during bond breaking
74 at the ether oxygen.^{25,31,34} Bond-breaking then leads to electrostatic stabilization of active
75 site residues, lowering the activation energy. Subsequent QM/MM and QM-cluster model
76 calculations have provided evidence that catalysis is due to both near attack conformation
77 and transition state stabilization, but with TSS being the main driving force of the proposed
78 mechanism.^{21,22,35}

79 While computational enzymology has advanced rapidly over the last two decades,^{6,36–38}
80 one persistent challenge in this research area is designing effective QM-regions that reliably
81 predict catalytic activity, with kinetic and thermodynamic properties that can converge
82 quickly with respect to model size. *Ad hoc* methods of selecting residues for inclusion in
83 the QM regions of QM/MM models or in QM-cluster models are poorly reproducible and

84 not well calibrated. One technique for QM region selection is to include all residues that
85 are within a specific radial distance from the center of the active site or from the center of
86 mass of the substrate. This construction paradigm is based on the idea that spherical active
87 site models are appropriate. Several studies by our group and others reveal that this is not
88 always the case,^{3,4,39–46} though CM active sites are known to be fairly compact and spherical.

89 To facilitate improved benchmarking in computational enzymology, our group has created
90 the *RINRUS* software toolkit to automate the process of generating QM-cluster models. Our
91 goal is to address various community-wide challenges in computational enzymology, such
92 as standardizing QM-cluster (and eventually QM/MM) model construction, lowering the
93 learning curve for new users, and reducing trial and error caused by *ad hoc* model-building
94 schemes. *RINRUS* uses an automated approach to trim and cap the active site fragments.
95 With a given protein structure and a user-defined “seed”, which consists of the substrate
96 and any active site fragments necessary to describe the chemical reaction, *RINRUS* identifies
97 proximal fragments that have important non-covalent interactions with the seed using the
98 graph theory concept of the Residue Interaction Network (RIN).^{47,48}

99 To summarize the *RINRUS* procedure, a protein structure is converted into a RIN graph
100 composed of only a subset of the fragments (referred to as “nodes” in graph theory) that have
101 an identifiable electrostatic and/or steric interaction (referred to as “edges” in graph theory)
102 with the seed nodes.^{47,48} The RIN is then processed using one or more user-selected schemes
103 that identify qualitative interaction types (Structural Interaction Fingerprints, SIFs)⁴⁹ or
104 quantitative schemes that utilize first-principles interaction energies like symmetry-adapted
105 perturbation theory (SAPT or F/I-SAPT, see below).^{50–53} *RINRUS* can also be used to rank
106 fragments via distance-based criteria. Once a ranking scheme is chosen and fragment rank is
107 enumerated, *RINRUS* will algorithmically construct QM-cluster models and provide input
108 files formatted appropriately for several commercial and open-source quantum chemistry
109 software packages.

110 This work has two major objectives. First, we analyze how specific residues influence the

enzymatic reaction and contribute to the convergence of *RINRUS*-built QM-cluster models of chorismate mutase. Multiple fragment ranking schemes are explored and compared, with models built incrementally, growing by one fragment at a time. Second, we explore QM-cluster modeling in a quasi time-dependent fashion by sampling MD snapshots with refined QM-cluster models to account for conformational averaging. Thermally stable conformational change is one of the most important aspects of regulating protein structure and activity, and conformational sampling of enzymes is typically probed on the micro-second time scale via MD simulations.⁵⁴ We have selected 250 snapshots from a 20 ns MD simulation of BsCM and processed each with *RINRUS* to obtain 250 different QM-cluster models. The catalytic transition state for each of the 250 QM-cluster models is optimized, and via computation of the connected reactant and product structures, kinetic and thermodynamic data is obtained.

Methods

All computations were based on the X-ray crystal structure of the *Bacillus subtilis* chorismate mutase taken from PDB entry 2CHT. The 2CHT enzyme is trimeric with three active sites formed at the interface of adjacent monomer chains. The active site of the crystallographic A/C chain was used for QM-model construction in this work. Further justification of using the chain A/C interface is provided in the Supporting Information. Hydrogen atoms were added to the enzyme using the *reduce* program.⁵⁵ For all QM-cluster models and MD simulations, the TSA found in the crystallographic active sites was replaced with the native substrate (chorismate).

Incremental QM-cluster model building with *RINRUS*

RINRUS identifies and ranks inter-residue interactions based upon two existing packages that compute the RIN and output node/edge information in machine and human-readable

135 formats. *Probe*⁵⁶ rolls a small sphere over the internal van der Waals surface of a protein
136 structure to identify and classify non-covalent interatomic interactions between fragments of
137 a protein structure; *arpeggio*⁵⁷ uses interatomic distance and angle criteria to identify and
138 classify interactions. Throughout this work, “seed”, “substrate”, and “ligand” synonymously
139 refer to the chorismate molecule shown in Figure S1.

140 A good fragment ranking scheme is needed to design reliable QM-cluster models, which
141 is a core feature of the open-source *RINRUS* package.⁵⁸ There are three different fragment
142 ranking schemes being tested in this work. The *RINRUS-probe* workflow ranks the impor-
143 tance of active site fragments based on the number of contact counts between each fragment
144 and the seed. When incrementally building models, fragments (categorized as residue side
145 chains, residue main chains, or solvent water molecules) are added to the model one at a time
146 in order from the fragment with the highest number of contacts with substrate to the low-
147 est. While *probe* parses interaction types into five simple SIF categories, *arpeggio* classifies
148 fourteen different chemical interaction type, based on the CREDO set of protein-substrate in-
149 teractions.⁵⁹ While *arpeggio* also accounts for typical interaction types like hydrogen bonding
150 and hydrophobic contacts, it can also more flexibly account for weaker inter-residue inter-
151 actions such as aromatic π -stacking or less common interactions such as halogen bonds. It
152 should be noted that the proximal interactions computed by *arpeggio* are ignored in this
153 study because the focus is on fragments that have recognized intermolecular forces with the
154 chorismate substrate, rather than distance-based metrics.

155 Symmetry adapted perturbation theory (SAPT) has become an increasingly popular
156 approach for computing non-covalent interaction energies between two molecules or frag-
157 ments.^{50–52,60–63} SAPT calculations are especially useful in that the interaction energies are
158 readily decomposed into electrostatic, exchange-repulsion, induction, and dispersion com-
159 ponents. Functional-group SAPT (F-SAPT)⁵² is an extension of SAPT that provides an
160 effective secondary two-body partition of the SAPT components. This additional partition-
161 ing allows computation of interaction energy between a fragment A (in this case study, the

162 chorismate ligand) and user-defined sub-fragments of a fragment B (the various side chain
163 and backbone fragments of the active site). F-SAPT is leveraged to decompose the interac-
164 tion energy between chorismate and individual residue main chains or side chains, without
165 cutting or capping fragments differently from what is used in the parent QM-cluster models.
166 We will use the F-SAPT interaction energies between chorismate and surrounding residue
167 fragments to rank incremental QM-cluster model building. This work uses the zeroth-order
168 formulation of F-SAPT, F-SAPT0, described by the equation:

$$E_{int} = E_{elec}^{(1)} + E_{exh}^{(1)} + [E_{ind}^{(2)} + E_{exch-ind}^{(2)} + \delta E_{HF}^{(2)}]_{ind} + [E_{disp} + E_{exch-disp}^{(2)}]_{disp} \quad (1)$$

169 F-SAPT0 computations employed the jun-cc-pVDZ basis set^{51,52} for all atoms and frozen core
170 electrons via the *PSI4* v1.3 package.⁶⁴ The jun-cc-pVDZ basis set has been demonstrated
171 to provide reliable SAPT interaction energies.⁶⁵

172 In recent work, a poor correlation between number of probe contacts and F-SAPT inter-
173 action energies was observed.^{66,67} We then hypothesized that F-SAPT interaction energies
174 will be a more quantitatively reliable metric for ranking the importance of active site residues.
175 However, SAPT calculations are computationally expensive (days of CPU time) compared
176 to the near-negligible effort required to compute and parse a RIN from *probe* or *arpeggio*
177 ranking (< 20 seconds of CPU time).

178 QM-cluster models were generated using the *RINRUS* software.⁵⁸ Trimming of residue
179 fragments is performed algorithmically by *RINRUS* depending on if the backbone NH, back-
180 bone CO, and/or side chain of a residue has interatomic contacts with chorismate. Where
181 covalent bonds are broken in the trimming procedure (typically across C_α atoms), *RINRUS*
182 automatically adds hydrogen atoms to satisfy carbon valency. We refer throughout to the
183 QM-cluster model that contains all fragments with a quantifiable interaction with the cho-
184 rismate ligand as a “maximal model”. Trimming details for the maximal model of the X-ray
185 crystal structure active site are shown in Table S1. To maintain the general shape and mimic

186 the semi-rigid character of the protein tertiary structure, all C_α atoms, along with the C_β
187 atoms of any Arg, Lys, Glu, Met, Trp, and Phe side chains were frozen to their crystallo-
188 graphic positions (if obtained from the X-ray crystal structure) or frozen at their positions
189 in the respective MD frame (if obtained from MD simulation). All chorismate atoms were
190 unconstrained in the QM-cluster model computations.

191 The QM computations were carried out using the Gaussian16 software package.⁶⁸ The
192 geometries of the models were optimized using density functional theory (DFT) with the
193 B3LYP exchange-correlation functional.^{69,70} The 6-31G(d') basis set was used for N, O, and
194 S,⁷¹ and the 6-31G basis set was used for C and H atoms.⁶⁰ The Grimme D3 (Becke-Johnson)
195 dispersion correction (GB3BJ) was also included,⁷² along with a conductor-like polarizable
196 continuum model (CPCM) using UAKS sets of atomic radii, a non-default electronic scaling
197 factor of 1.2, and default cavity parameters for water but with an attenuated dielectric
198 constant of $\epsilon = 4$.^{73,74} Transition states were located for the elementary step of the proposed
199 mechanism, and the reactants and products were then confirmed by following the intrinsic
200 reaction coordinate (IRC).¹ The zero-point energies (ZPE) and thermal enthalpy/free energy
201 corrections were calculated at 1 atm and 298.15 K.

202 MD trajectory-based QM-cluster models

203 For the MD simulations, some pre-processing of the X-ray crystal structure was necessary.⁶⁷
204 Missing residues in the 2CHT X-ray crystal structure were added from the C-terminus using
205 PDB entry 1DBF,⁷⁵ a BsCM structure without substrate or TSA in complex with the protein.
206 The two structures were globally aligned and atomic coordinates from 1DBF were added
207 to the 2CHT structure based upon the point where the two structures begin a common
208 structural alignment. Specifically, residues 1 and 116-127 from 1DBF were added to 2CHT
209 for chain A, residues 1 and 115-127 were added for chain B, and residues 1-2 and 115-127

¹It is important to note that our group employs the “freeze code” scheme in Gaussian16, in which all Hessian elements are zero when two frozen Cartesian coordinates are involved. The phenomenon in which several small magnitude imaginary vibrational frequencies appear in thermochemical analysis does not occur in our treatment of the Hessian matrix.

210 were added for chain C (with residues 2 and 115-119 of 2CHT chain C being replaced with
211 the corresponding coordinates from 1DBF). Hydrogen atoms were added to this structure
212 via the H++ server using default parameters.⁷⁶ The native substrate chorismate in a pre-
213 reactive conformation was used in MD simulations instead of the TSA. The AMBER18 MD
214 package⁷⁷ was used to run the MD simulations, and the AMBER force field ff14SB was used
215 with periodic boundary conditions and a cutoff value of 9 Å for non-bonded interactions.
216 The Antechamber package was employed to parameterize the chorismate substrate with the
217 Generalized Amber Force Field (GAFF).^{77,78} The protonated structure with chorismate was
218 solvated in a cubic 10 Å box of water with the explicit solvent model TIP3P.⁷⁹ The MD
219 model charge was neutralized by adding 9 Na⁺ ions.⁸⁰

220 An energy minimization of the system was first carried out with protein heavy atoms
221 constrained to their crystallographic coordinates using a harmonic positional restraint (k_{pos})
222 of 200 kcal mol⁻¹/Å² allowing the solvent bath to be initially relaxed and the hydrogen
223 bonding networks to be established. The protein heavy atom constraints were then iteratively
224 relaxed over five 20 ps simulations using Langevin dynamics under constant-temperature,
225 constant-pressure (NPT) conditions at 300 K and 1 atm; the SHAKE algorithm⁸¹ was used
226 to constrain all bonds involving hydrogen atoms for the initial equilibration simulation. The
227 protein was then allowed to move freely for a 20 ns production-level run. The timescale of
228 each frame was 1 ps, for a total of 20,000 frames. The protein RMSDs of MD trajectories
229 were calculated using the *cpptraj* module of AMBER18.⁸²

230 Schemes for selection of frames for the QM-cluster models from 231 MD trajectories

232 Designing QM-cluster models from a large number of MD frames will allow consideration
233 of conformational influence on kinetic and thermodynamic quantities. Eight schemes are
234 considered in an attempt to cover a diverse sampling of conformations and non-equilibrium
235 structures. From each scheme, 20 to 40 MD frames are selected and then used to construct

236 a QM-cluster model of the active site. The first scheme considered (\mathbf{S}_1) is perhaps the most
237 common scheme for MD simulation sampling, and involves selecting MD frames at equal
238 intervals over the course of an equilibrated simulation. This approach is effectively random
239 and unbiased. For the next set of schemes (\mathbf{S}_2 , \mathbf{S}_3 , and \mathbf{S}_4) we chose frames similar to the X-
240 ray crystal structure. Furthermore, it may be better to consider only the structural variations
241 of the active site residues rather than of the whole protein, and this idea is incorporated into
242 \mathbf{S}_3 , \mathbf{S}_4 , \mathbf{S}_6 , \mathbf{S}_7 , and \mathbf{S}_8 . For the final set of schemes (\mathbf{S}_5 , \mathbf{S}_6 , \mathbf{S}_7 , and \mathbf{S}_8) frames were grouped
243 by a specific metric and then k-means clustering divided the frames into 3 or 4 clusters. These
244 schemes should increase the structural diversity of QM-cluster model refinement. Again, note
245 that the Chain A/C interface was used to construct the QM-cluster models from each selected
246 MD frame. Detailed frame selection criteria are as follows.

247 \mathbf{S}_1 - Twenty frames were selected from the MD simulation at equal intervals of 1,000 ps
248 over the entire 20 ns equilibrated simulation.

249 \mathbf{S}_2 - The RMSD of the backbone atoms (C, O, C_α , N, and H) of the entire protein
250 structure compared to the X-ray crystal structure was measured for each frame. Frames
251 with an RMSD within ± 1 standard deviation (0.76 \AA) of the mean RMSD (2.66 \AA) were
252 isolated, and a random number generator was used to select 30 frames from this data set.

253 \mathbf{S}_3 - The RMSD of the backbone atoms of a selection of active site residues compared to
254 the X-ray crystal structure was measured for each frame. The subset of active site residues
255 was defined as all residues present in any of the QM-cluster models obtained from \mathbf{S}_1 : Arg7,
256 Glu78, Arg90, Tyr108, Leu115, Phe57, Ala59, Lys60, Arg63, Val73, Thr74, and Cys75.
257 Frames with an active site backbone RMSD within ± 1 standard deviation (0.09 \AA) of the
258 mean RMSD (0.84 \AA) were isolated, and a random number generator was used to select 30
259 frames from this data set.

260 \mathbf{S}_4 - This scheme used the RMSD of the side chain atoms of the active site residues (listed
261 in \mathbf{S}_3) compared to the X-ray crystal structure. Frames with a side chain backbone RMSD
262 within ± 1 standard deviation (0.16 \AA) of the mean RMSD (1.66 \AA) were isolated, and a

263 random number generator was used to select 30 frames from this data set.

264 \mathbf{S}_5 - The RMSD of all heavy (non-hydrogen) atoms of protein and chorismate compared
265 to the X-ray crystal structure was measured for each frame. K-means clustering was used
266 to group the frames into three distinct clusters based on the gap statistic and elbow plots
267 shown in Figure S2, and a random number generator was used to select 10 frames from each
268 of the three clusters.

269 \mathbf{S}_6 - The RMSD of the backbone atoms of only the active site residues (from \mathbf{S}_3) compared
270 to the X-ray crystal structure was measured for each frame. Based on analysis of the RMSD
271 using the gap statistic and elbow plots in Figure S3, it became apparent that there is only
272 one unique k-means cluster. We then subdivided the data into four clusters and randomly
273 selected 10 frames from each of the four clusters.

274 \mathbf{S}_7 - This scheme used the RMSD of the side chain atoms of the active site residues
275 compared to the X-ray crystal structure instead of the backbone atoms. Similar to \mathbf{S}_6 , k-
276 means clustering with the active site side chain atom RMSD values was not a useful technique
277 (Figure S4). The MD frames were still split into another four arbitrary clusters and randomly
278 selected to provide an unbiased sampling of 40 additional MD frames.

279 \mathbf{S}_8 - The number of *probe* contacts between chorismate and surrounding residues was
280 measured for each frame of the MD trajectory. K-means clustering grouped the frames into
281 distinct clusters. However, the gap statistics and elbow plots shown in Figure S5 indicate
282 our MD frames are not easily clustered into less than 10 sets, so the clustering is truncated
283 at $k = 3$. A random number generator was used to randomly select 10 frames from each of
284 the three clusters.

285 From the eight selection schemes, a total of 250 unique MD frames were chosen and
286 then refined into QM-cluster models generated by *RINRUS*. Note that the composition
287 of the QM-cluster models is not uniform. Each QM-cluster model constructed from MD
288 includes all fragments recognized by the *probe* software as having inter-residue interactions
289 with chorismate *for that specific MD frame*. Interestingly, nearly adjacent and even adjacent

frames that were selected by the various schemes showed non-uniform RIN composition [frames 159 (\mathbf{S}_8) and 161 (\mathbf{S}_7); 1218 (\mathbf{S}_6) and 1221 (\mathbf{S}_7); 2473 (\mathbf{S}_8) and 2475 (\mathbf{S}_6); 7603 (\mathbf{S}_6) and 7607 (\mathbf{S}_5); 9748 (\mathbf{S}_6) and 9750 (\mathbf{S}_2); 12378 (\mathbf{S}_6) and 12379 (\mathbf{S}_5), 19719 (\mathbf{S}_2) and 19721 (\mathbf{S}_7)]. Active site RIN composition of the adjacent frames 12378 and 12379 is shown in Table S2.

Results and Discussion

Building QM-cluster models with different ranking schemes

We began by examining how different schemes to prioritize residue interactions affect the construction of QM-cluster models and the convergence of predicted reaction properties. Full information about model size, model charge, and kinetic and thermodynamic properties are provided for all iterative building schemes in Tables S1 and S3. Using the X-ray crystal structure, 12 QM-cluster models were built by incrementally adding one residue based on their cumulative *probe* contact counts with chorismate within the X-ray crystal structure. The maximal *probe*-derived model, which includes all residues with any *probe* contact with the chorismate, contains 203 atoms and is shown in Figure 1.

The computed ΔG^\ddagger and ΔG_{rxn} values for the Claisen rearrangement reaction are plotted in Figure 2 for the *probe*-based model building scheme. First, the highest *probe*-ranked fragment, Phe57 side chain, is added to the chorismate to constitute the first QM-cluster model, containing 42 atoms and a total model charge of -2. The second QM-cluster model is generated by adding the Arg7 side chain to the first model. The second model now contains 64 atoms and a total model charge of -1. The list of fragments provided in Table S1 gives details about subsequent models, culminating in our "maximal model" of 203 atoms.

For this study, we define models as being converged for a given building scheme if *both* ΔG^\ddagger and ΔG_{rxn} of a model *and all subsequent larger models* are within ± 1 (tight convergence criteria) or ± 3 kcal mol⁻¹ (loose convergence criteria) of their reference values (ΔG^\ddagger and

315 ΔG_{rxn} of the maximal model), respectively. The maximal *probe*-based *RINRUS*-designed
316 QM-cluster model has values of $\Delta G^\ddagger = 9.1$ kcal mol⁻¹ and $\Delta G_{rxn} = -16.3$ kcal mol⁻¹. As the
317 size of the model increases, the predicted ΔG^\ddagger and ΔG_{rxn} become converged at the 155-atom
318 model within the defined metric of convergence of ± 3 kcal mol⁻¹, after Arg63 was added to
319 the 133-atom model. None of the *probe* models converge both ΔG^\ddagger and ΔG_{rxn} to within 1.0
320 kcal mol⁻¹ of the maximal QM-cluster model. Overall, the ΔG_{rxn} value qualitatively agrees
321 with other QM-cluster model and QM/MM studies of the chorismate mutase catalytic step
322 that exhibited strongly exergonic reaction free energies.^{5,12,16,22,35,83,84} Below, we will explain
323 why the computed ΔG^\ddagger of converged and maximal QM-cluster models is significantly lower
324 than the known experimental value.

325 The *Arpeggio* interaction classification may be more robust than *probe* in that it is not
326 inherently limited to only the local interatomic contacts. Indeed, all residues identified in
327 the *probe* ranking scheme are included in the *arpeggio* ranking scheme in addition to Glu78,
328 as well as the side chains of Val73, where only backbone atoms had been included in the
329 *probe*-based models as shown in Table S4. Due to differences in which specific residue atoms
330 interact with chorismate, some fragments in the *arpeggio*-based models are trimmed and
331 capped differently. Additional details of the *arpeggio* trimming scheme are shown in Table
332 S1. The maximal *arpeggio*-based model has 245 atoms, which makes it somewhat larger than
333 the maximal *probe*-based model (203 atoms). Figure 3 shows the computed values of ΔG^\ddagger
334 and ΔG_{rxn} when employing the *arpeggio*-based RIN to construct the QM-cluster models.
335 The maximal *arpeggio*-based model (used as the reference for convergence tests) has $\Delta G^\ddagger =$
336 10.2 kcal mol⁻¹ and $\Delta G_{rxn} = -16.1$ kcal mol⁻¹.

337 *Arpeggio*-based models predict satisfactory convergence for ΔG^\ddagger and ΔG_{rxn} (Figure 3,
338 magenta plot) once QM-cluster models are larger than 200 atoms. However, we see a dra-
339 matic disruption of convergence in the reaction free energy when Thr74 is added to form
340 the 136-atom model. The computed ΔG_{rxn} of -36.3 kcal mol⁻¹ is artificially too negative
341 because the chorismate translates far out of the active site in the optimized product struc-

342 ture. Once Arg90 is added to form the 158-atom model, the chorismate is properly posed;
343 all substrate-arginine hydrogen bonds seen in the maximal model are accounted for. While
344 no *arpeggio*-based models have both ΔG_{rxn} and ΔG^\ddagger converged within ± 1 kcal mol⁻¹ of
345 the maximal model, convergence to the looser ± 3 kcal mol⁻¹ threshold appears once the
346 177-atom model is constructed.

347 One limitation with the *arpeggio* scheme is the more frequent occurrence of tie scores
348 for the number of interaction counts. While the number of *probe* contacts can vary over
349 3–4 orders of magnitude as it is linked to the continuous inter-residue surface area, *arpeggio*
350 interaction count scores will be much smaller as values arise from summing the categorical
351 presence/absence of interaction types. The *RINRUS* code does not yet preferentially discern
352 between fragments with tied rankings, so there is no chemical significance to the output
353 ordering for those residues. However, depending on which residues are selected in a tie
354 situation, the convergence of ΔG^\ddagger and ΔG_{rxn} values can be affected.

355 In situations where there is a tie in the number of *arpeggio* contact counts, we have
356 manually reordered the *RINRUS* ranking list. First, the number of *arpeggio* contact types
357 are used to break the tie. However, if there are fragments where the number of contact
358 types is also tied, the following convention was used to manually prioritize ranking: charged
359 residues > polar > non-polar residues. In situations where there is still a tie between residues
360 of the same category, the *probe*-based contact count ranking was used to break the tie, as
361 in the case of Thr74 being added before Tyr108. Improvements to the *RINRUS* code to
362 automatically account for tie-breaking in either *probe* or *arpeggio* rankings are currently
363 in development. Further details about *probe*, *arpeggio*, and tie-broken *arpeggio* QM-cluster
364 models is given in Table S1.

365 The tie-broken *arpeggio*-based models (Figure 3, brown plot) show quicker convergence
366 to the ΔG^\ddagger value of the maximal model (10.2 kcal mol⁻¹) than in the original *arpeggio*
367 building scheme. Adding Arg90 before Thr74 via the tie-breaking scheme also eliminates
368 the odd disruption of ΔG_{rxn} convergence. However, there is still no model where both the

369 ΔG_{rxn} and ΔG^\ddagger are converged to within ± 1 kcal mol⁻¹ of the maximal model. Tie-broken
370 *arpeggio*-based models have kinetic and thermodynamic values converging to the loose ± 3
371 kcal mol⁻¹ threshold starting with the 191-atom model. The tie-broken models do not have a
372 significant effect on kinetic or thermodynamic convergence beyond fixing the spurious ΔG^\ddagger
373 value. However, avoiding random ordering of fragments that have tied contact count or
374 contact type values seems prudent until an automated approach is available.

375 A third scheme using quantitative chorismate-residue interaction energies as a ranking
376 method was evaluated. As observed in previous work,^{66,67} the F-SAPT interaction energies
377 prioritize important charged residues which play a key role in transition state stabilization.
378 Our analysis of several proteins (including chorismate mutase) indicated no apparent corre-
379 lation between number of *probe* contact counts and E_{int} between noncovalently interacting
380 biochemical fragments, raising concern that *probe* may de-emphasize residues that have a
381 strong, but directional electrostatic interaction with seed fragments. The substrate-residue
382 interaction energies were computed using F-SAPT0, and a series of 11 QM-cluster mod-
383 els were first constructed by adding fragments ranked from largest negative E_{int} with the
384 chorismate substrate to the largest positive E_{int} value (Table S5). It must be recognized
385 that a negative total F-SAPT interaction energy signifies a favorable interaction between a
386 residue fragment and chorismate, while a positive total F-SAPT interaction energy describes
387 a repulsive interaction. Given a dianionic chorismate substrate, it was expected that posi-
388 tively charged residues will be ranked first, then polar residues, then nonpolar residues, then
389 negatively charged residues. The initial F-SAPT scheme ranked the four positively charged
390 residues highest; Arg7 is first ($E_{int} = -140.5$ kcal mol⁻¹), followed by Arg63 ($E_{int} = -133.2$
391 kcal mol⁻¹), then Arg90 ($E_{int} = -113.0$ kcal mol⁻¹), and Lys60 ($E_{int} = -78.1$ kcal mol⁻¹). For
392 comparison to a few polar residues, the E_{int} of Tyr108 and Thr74 are -15.5 kcal mol⁻¹ and
393 +10.9 kcal mol⁻¹, respectively.

394 Matching literature precedence, the *probe* and *arpeggio* schemes for constructing QM-
395 cluster models frequently de-prioritize charged residues compared to F-SAPT.⁶⁷ While Arg7

396 is ranked first or second in all three schemes, Arg90 is ranked 3rd by F-SAPT, 5th by
397 *probe*, and 6th by *arpeggio*, as illustrated in Tables S4 and S3. Arg63 (1st by F-SAPT) was
398 ranked 8th by *probe* and 3rd by *arpeggio*. A visual relationship between *probe* contacts and
399 the orientation of important charged active site arginine residues can be seen in Figure S6.
400 Phe57 is ranked first in the *probe* ranking scheme with a total of 288 contacts with chorismate
401 (highlighted in grey in Figure S6), but only has an F-SAPT E_{int} of -2.0 kcal mol $^{-1}$ and is
402 ranked 10th. Arg63 has only 97 *probe* (highlighted in yellow) interaction counts, making
403 it the 8th ranked fragment, but again has the second largest negative F-SAPT interaction
404 energy. Charged active site amino acid residues are crucial for both NAC and TSS of
405 the chorismate substrate. Yet Arg7 is the only one of four positively charged residues in
406 the BsCM active site that is ranked consistently high in the *probe*, *arpeggio*, and F-SAPT
407 schemes. Our F-SAPT results strongly suggest large residue side chains can be oriented in
408 such a way that they provide strong hydrogen bonds within an active site, but have low RIN
409 contact count values.

410 In a recent analysis of glycine-N-methyltransferase,⁸⁵ we recognized that residues with
411 strongly unfavorable (positive) interaction energies should be ranked higher than residues
412 with near-zero F-SAPT interaction energies. Ranking fragments by $|E_{int}|$ will thus prioritize
413 negatively charged active site fragments that have a large, but unfavorable interaction with
414 the dianionic substrate before fragments that have a small or negligible interaction with the
415 substrate. Semantically, the difference between F-SAPT schemes is subtle, but the quality
416 of QM-cluster models could be substantially affected by this choice. The ΔG^\ddagger and ΔG_{rxn}
417 values for the two F-SAPT ranking schemes (signed in magenta and unsigned in brown) are
418 overlaid in Figure 4. Both schemes overlap until the 139-atom model, where Ala59 is next
419 added in the signed scheme and Thr74 is added in the unsigned scheme.

420 As the F-SAPT calculations were derived from the maximal *probe* model, the *probe*,
421 signed and unsigned F-SAPT schemes will all have an equivalent maximal model ($\Delta G^\ddagger =$
422 9.1 kcal mol $^{-1}$ and $\Delta G_{rxn} = -16.3$ kcal mol $^{-1}$) that does not need to be recomputed. The

423 unsigned F-SAPT ranking scheme exhibits slightly improved convergence over the signed
424 scheme, as the last three unsigned models were within ± 3 kcal mol⁻¹ of the maximal model
425 for both ΔG^\ddagger and ΔG_{rxn} values (Table S3). Despite the expectation that QM-cluster models
426 derived from F-SAPT rankings would be optimal, none of the truncated F-SAPT models
427 are within ± 1 kcal mol⁻¹ of both the ΔG^\ddagger and ΔG_{rxn} values. Thus, there is little quali-
428 tative difference between the largest QM-cluster models built with the F-SAPT, *probe*, or
429 *arpeggio* ranking schemes. The F-SAPT scheme is also quite computationally expensive on
430 the front end compared to *probe* and *arpeggio* schemes. Generally, only QM-cluster models
431 of chorismate mutase that closely resemble the maximal models are reliable. To ascertain
432 how more liberally truncated models can appropriately reproduce NAC or TSS phenomena,
433 a brute force or combinatorial approach (like the RINRUS-based investigation of Catechol-
434 O-Methyltransferase)⁴ would need to be carried out on the chorismate mutase active site.

435 Previous enzymology studies done by our group have shown that B3LYP generally under-
436 estimates free energies of activation compared to experiment.^{2-4,85} Accordingly, all ranking
437 schemes had maximal QM-cluster models of the chorismate mutase active site that exhibited
438 ΔG^\ddagger values significantly lower than the experimental value⁸⁶ of 15.4 ± 0.5 kcal mol⁻¹. The
439 maximal F-SAPT / *probe*-based model predicted an activation free energy of 9.1 kcal mol⁻¹,
440 while the maximal *arpeggio*-based model predicted 10.2 kcal mol⁻¹. QM-cluster models
441 reported by Burschowsky and coauthors at the B3LYP/6-31G(d)//B3LYP/6-311+G(d,p)
442 level of theory arrived at an even lower ΔG^\ddagger value for the chorismate mutase catalysis (8.6
443 kcal mol⁻¹).³⁵ It is important to stress that this work is not concerned with accuracy of the
444 QM-cluster models, but focused on understanding how kinetics and thermodynamics are
445 influenced by the decisions involved in QM-cluster model construction.

446 Our lab (and others) are exploring much-needed benchmarks of one-electron basis set
447 and density functional on enzyme models.^{45,46,87-92} To avoid model construction contribut-
448 ing to kinetic and thermodynamic errors, the current study demonstrates that QM-cluster
449 models require, at minimum, over ~ 150 atoms. This lower bound to model size unfor-

450 tunately guarantees that employing large basis sets and double-hybrid density functionals
451 will be intractable for most production-level exploration of enzyme chemical mechanisms.
452 Ideally, the community will arrive at a consensus on methodological best practices in QM-
453 cluster modeling to accurately and efficiently compare to experimental observation. Until
454 then, dispersion-corrected B3LYP with small Pople-style basis sets is an efficient and mostly
455 reliable level of theory for calibrating the error arising from QM-cluster model composition.

456 **Building QM-cluster models from MD frames**

457 Next, we explore the impact that fluctuations of residue and substrate positioning can have
458 on both the design of QM-cluster modeling and the resulting kinetic and thermodynamic
459 properties. First, 250 frames from a 20 ns MD simulation of solvated chorismate mutase
460 were sampled to construct maximal QM-cluster models of the active site using *probe* contacts.
461 Structures from MD simulations can be advantageous over crystallographic structures in their
462 unambiguous hydration shells and energy relaxation of the active site structure based on *in*
463 *vivo* substrates rather than inhibitors or transition state analogues. However, building QM-
464 models from MD simulations will incorporate statistical uncertainty, as sampling many MD
465 frames are required to represent the diversity of structural conformations.^{93–95} In particular,
466 we examine three features particularly relevant for QM-cluster modeling that are expected to
467 cause variation in the predicted reaction properties: 1) the number and identity of residues
468 included in the model, 2) the number of waters included in the model, and 3) the statistical
469 ensemble of sampled frames.

470 In plotting the activation and reaction free energies for all 250 MD-derived QM-cluster
471 models (Figure 5, Figure S7, and Table 1), there is a wide range of values wherein the
472 mean activation free energy is 10.3 ± 2.6 kcal mol⁻¹ and the mean free energy of reaction
473 is -15.4 ± 3.4 kcal mol⁻¹. These ranges encompass the converged values observed for QM-
474 cluster models built from the X-ray crystal structure, though this is unsurprising given the
475 large standard deviation observed in the ensemble of refined MD frames. The size of the

476 maximal QM-cluster models ranges from 158 to 240 atoms, with the five smallest models
477 containing only 8 residues and 5 or 6 waters and the largest model containing 13 residues
478 and 3 waters.

479 Using *probe* to identify active site fragments, a total of 22 residues were identified as
480 having at least one contact interaction with the substrate in at least one frame over the course
481 of the entire MD simulation. Table S6 shows the mean interaction counts of each identified
482 residue with chorismate. There is precedence that crystal packing leads to an increase in
483 protein-substrate contact counts.^{67,96} However, replacement of the TSA with chorismate in
484 the X-ray crystal structure without a subsequent geometry relaxation does not create steric
485 clashes with the protein, which might have nonphysically amplified the contact counts. As
486 expected, the Arg90 and Arg7 residues have the highest mean contact counts, 116.3 and
487 78.3, respectively. Several residues appear in RINs during the entire MD run with very low
488 mean interaction counts (< 0.02) such as Ala9, Pro117, and residues 242-245. None of these
489 residues have inter-residue contacts with the TSA in the X-ray crystal structure. Pro117 is
490 the only “rare” residue from the entire MD simulation that also appears in the 250 selected
491 frames that were refined to QM-cluster models. The mean interaction counts of residues
492 modeled in the 250 QM-cluster models is similar to those observed in the 20000 RINs of
493 the MD simulation (Table S6). This similarity affirms that the selection schemes used to
494 refine MD frames into QM-cluster models are representative of the entire MD simulation.
495 From Tables S6 and S7, we find that consistently high-ranking active site residues common
496 to *probe*, *arpeggio*, and F-SAPT schemes can occasionally be missing entirely from specific
497 MD frames.

498 Surprisingly, QM-cluster models with atypical composition do not necessarily create ki-
499 netic or thermodynamic outliers. Frame 394 is the only member of the 250-frame subset to
500 not have any *probe* contacts with the Arg90 side chain. It also does not contain an Arg63
501 fragment, making it the only QM-cluster model with net -2 charge. The missing fragments
502 result in a spuriously high free energy of activation (see below). The QM-cluster models

503 made from frames 9464, 14007, 16450 are the only three of the 250 that have no *probe* con-
504 tacts between substrate and Leu115, yet all three have kinetic/thermodynamic properties
505 within the uncertainty range of the total set. Frames with rare residues have a small impact
506 on the overall kinetic and thermodynamic values. For example, the five QM-cluster models
507 that contain Pro117 have mean ΔG^\ddagger and ΔG_{rxn} values of 11.2 ± 2.9 kcal mol⁻¹ and $-15.1 \pm$
508 4.3 kcal mol⁻¹, respectively.

509 Mean *probe* contact counts of the 250 QM-cluster models arising from MD sampling em-
510 phasize charged residues more than the X-ray crystal structure, but interestingly, Figure S8
511 still shows a lack of correlation with F-SAPT $|E_{int}|$ values computed at the X-ray crystal
512 structure. MD-averaged *probe* counts rank the first five residues as Arg90, Arg7, Leu115,
513 Ala59, and Arg63. The Lys60 residue has a mean contact count of only 2.9, but as demon-
514 strated earlier, has the 4th-largest $|E_{int}|$ with the substrate. The mean *probe* contact counts
515 for Leu115 are large (72.3), but it has the smallest absolute F-SAPT interaction energy.
516 Of the uncharged side chain fragments, Tyr108 has the smallest mean *probe* count (28.8)
517 and the largest $|E_{int}|$ value. These conflicting results demonstrate how various schemes rank
518 residue importance differently. Great challenges remain in quantifying the impact of specific
519 amino acid fragments on protein-substrate reactivity.

520 The catalytic activity of chorismate mutase is particularly driven by charge stabilization
521 interactions, which might be susceptible to differences in net model charge. Thus, it is of
522 interest to examine whether differences in model charge of QM-cluster models refined from
523 individual MD frames can account for the broad range of activation and reaction free energies
524 observed. Figure 6 shows the distribution of the net model charges for the 250 QM-cluster
525 models compared to the range of ΔG^\ddagger and ΔG_{rxn} values for each model. The net charge of
526 our 250 QM-cluster models varies from -2 to +2, with the majority (200 models) having an
527 overall neutral charge. QM-cluster models with a neutral model charge had mean ΔG^\ddagger and
528 ΔG_{rxn} values of 10.1 ± 2.4 and -15.7 ± 3.3 kcal mol⁻¹, respectively. Only one MD-based
529 QM-cluster model (frame 394) has a -2 net charge model and it provides anomalously high

530 values of ΔG^\ddagger and ΔG_{rxn} , 20.0 and -7.7 kcal mol⁻¹, respectively. The outlying energetics of
531 frame 394 are likely due to missing Arg90 and Arg63 fragments, which have proven to be
532 critical for the enzyme catalysis.^{19,31} The 33 QM-cluster models with net +1 charge show
533 the largest range of ΔG^\ddagger values, encompassing the highest (19.1 kcal mol⁻¹, frame 4114)
534 and lowest (4.1 kcal mol⁻¹, frame 8310) values. However, the mean energetic values are in
535 reasonable agreement with the complete set, 11.1 ± 3.6 kcal mol⁻¹ for ΔG^\ddagger and $-14.0 \pm$
536 3.3 kcal mol⁻¹ for ΔG_{rxn} . The net charge of the QM-cluster models do not systematically
537 influence the ΔG^\ddagger and ΔG_{rxn} values.

538 We have shown the maximal QM-cluster models based on the X-ray crystal structure,
539 from any of our building schemes, are expected to provide kinetics and reaction thermody-
540 namics that are reliably converged at a given level of theory (Figure 2). The 250 maximal
541 QM-cluster models derived from MD will have significant variations in the residues that are
542 included in each RIN. This heterogeneity opens the question: when comparing QM-cluster
543 models with the same fragment composition but with different active site conformation
544 and/or relative frozen atom positions, will the computed reaction kinetics and thermody-
545 namics show consistent values or large variance? To disentangle model composition from
546 model structure, the dataset is trimmed to only include MD-derived QM-cluster models
547 that have an identical composition. This data filtering ignores distinguishing models with
548 different water molecule positioning. The subset contained 144 total models in 37 different
549 bins (Figure S9). Among the groups of models with identical designs but taken from different
550 snapshots, the groups still show a wide distribution of ΔG^\ddagger and ΔG_{rxn} values, with ranges
551 from 4.1 to 16.4 kcal mol⁻¹ for ΔG^\ddagger and -28.8 to -6.7 kcal mol⁻¹ for ΔG_{rxn} . No patterns seem
552 to emerge from this data. If the bins in Figure S9 showed a narrow distribution of kinetics
553 and thermodynamics, we would conclude that the observed wide distribution of values in
554 the 250 QM-cluster models manifested from differences in active site fragment composition.
555 However, data in Figure S9 match the large variation of the total set of QM-cluster models
556 refined from the MD simulation. The variation must be due to conformational fluctuation

557 of active site residues and water molecules during the course of the MD trajectory.

558 The active site RIN from the X-ray crystal structure contains only a single crystallo-
559 graphically resolved water molecule shown to have interactions with the substrate captured
560 by *probe*. The chorismate mutase active site is small and quite solvent-exposed, but the lack
561 of crystallographically resolved water molecules is unsurprising (though rarely quantified in
562 the literature). The 3D protein structure is typically of greater interest than the poorly
563 resolved oxygen nuclei of the bulk solvent. In contrast, the QM-cluster models generated
564 from the MD simulation encompass a comprehensive hydration shell. In the 250 MD frames
565 selected for QM-cluster model refinement, 2 to 10 water molecules are identified by *probe*
566 as having an interaction with chorismate (Figure 7). Intriguingly, the *RINRUS*-built QM-
567 cluster models of chorismate mutase derived from MD frames have on average 5.6 water
568 molecules interacting with the substrate. Frame 6981 is the only QM-cluster model with 2
569 waters in the active site, and ΔG^\ddagger is predicted to be 10.8 kcal mol⁻¹. At the other extreme,
570 the two QM-cluster models with 10 waters have a mean ΔG^\ddagger value of 11.3 kcal mol⁻¹. Only
571 29 models total have 2, 3, 8, 9, or 10 water molecules in the RIN. Despite low occurrence in
572 the sampled MD frames, these models have mean predicted ΔG^\ddagger and ΔG_{rxn} values of 10.9
573 ± 3.0 kcal mol⁻¹ and -14.8 ± 2.9 kcal mol⁻¹, respectively; kinetics and thermodynamics are
574 within uncertainties of the total set of 250 models. The 221 QM-cluster models with 4 to
575 7 water molecules are qualitatively similar, 10.2 ± 2.6 kcal mol⁻¹ for ΔG^\ddagger and -15.4 ± 3.4
576 kcal mol⁻¹ for ΔG_{rxn} . Clearly, the number of waters in the BsCM active site has minimal
577 influence on the kinetic and thermodynamic properties of QM-cluster models. However, the
578 inclusion of *any type of water network* at the active site-solvent boundary in our MD-derived
579 QM-cluster models may be a factor in the ~ 2 kcal mol⁻¹ higher free energies of activation
580 observed compared to models constructed from the X-ray crystal structure.

581 Finally, we analyze groupings of the statistical ensemble of QM-cluster models (Table 1),
582 which showed minimal statistical difference with the overall mean kinetic and thermodynamic
583 values ($\Delta G^\ddagger = 10.3 \pm 2.6$ kcal mol⁻¹ and $\Delta G_{rxn} = -15.4 \pm 3.4$ kcal mol⁻¹). Schemes labeled

584 **XS**₂ to **XS**₈, are expanded versions of **S**₂ to **S**₈, and include all frames from the 250 QM-
585 cluster models that fit the criteria of each Scheme. For example, **XS**₂ includes the 30 frames
586 from **S**₂ and the additional 118 frames from the 250 frame set that have an RMSD within 0.76
587 Å of the mean backbone atom RMSD. Kinetic and thermodynamic results for the expanded
588 schemes are given in Table 2.

589 The first scheme, **S**₁, contains 20 frames and should be representative of a random and
590 unbiased distribution of activation and reaction free energies over the course of the entire
591 MD simulation. Mean ΔG^\ddagger and ΔG_{rxn} values of the 20 frames used in **S**₁ are lower than
592 the total set, but in reasonable agreement. Establishing that k-means clustering of **S**₆ and
593 **S**₇ was invalid, these two schemes also represent a random selection of frames. We combined
594 the frames of **S**₁, **S**₆, and **S**₇ (100 total) into an expanded Scheme (**S**₁ + **S**₆ + **S**₇) in Table
595 2. Interestingly, the kinetic and thermodynamic values of **S**₁ + **S**₆ + **S**₇ are within 0.10
596 kcal mol⁻¹ of the entire data set. This improved agreement suggests 20 randomly selected
597 frames (8% of the total data set) may not be a robust amount. Since most of the expanded
598 schemes have mean kinetic and thermodynamic values very similar to the total set of 250
599 MD frames, then a sample of 100 frames (40% of the data points in total set) may be an
600 upper bound needed to emulate the total set.

601 The next sets of schemes (**S**₂, **S**₃, and **S**₄), take into account the fluctuation of the active
602 site residues and discard MD frames geometrically dissimilar to the X-ray crystal structure.
603 All three schemes predict mean ΔG^\ddagger values slightly lower than the entire dataset. **S**₂ and
604 **S**₄ mean ΔG_{rxn} values are lower than the total mean, while the **S**₄ mean is slightly higher
605 than **S**₂ and **S**₃. The extended **XS**₃ and **XS**₄ schemes (Table 2) are closer to the total mean
606 statistics than **XS**₂.

607 The **S**₅ scheme used k-means clustering of the RMSDs (ranging from 1.46 to 4.22 Å
608 shown in Table S8) of the active site residues to group similar frames into clusters. The
609 three clusters for **S**₅ are ordered from largest centroid RMSD value (**S**₅-C₁) to the lowest
610 (**S**₅-C₃). The (**S**₅-C₁) and (**S**₅-C₃) clusters have nearly the same mean ΔG^\ddagger value, below

611 the mean ΔG^\ddagger value of the total data set. The (\mathbf{S}_5 - \mathbf{C}_2) cluster in contrast, is higher (11.0
612 kcal mol⁻¹) than the total data set. Values of ΔG_{rxn} become less negative as the centroid
613 RMSD value decreases from \mathbf{C}_3 to \mathbf{C}_1 , and the extended Scheme \mathbf{XS}_5 - \mathbf{C}_3 to \mathbf{XS}_5 - \mathbf{C}_1 follows
614 the same pattern. Scheme \mathbf{S}_5 gives a mean ΔG^\ddagger value closest to that of the total data set.
615 The mean ΔG_{rxn} value for \mathbf{S}_5 is also quite close, but effectively random sampling in \mathbf{S}_6 and
616 \mathbf{S}_7 give a slightly better match to the total set.

617 The last scheme (\mathbf{S}_8) classified MD frames with k-means clustering according to *probe*
618 interatomic contacts between the chorismate ligand and surrounding residues. All three
619 clusters of \mathbf{S}_8 predicted the mean ΔG^\ddagger value to be 0.46 - 1.15 kcal mol⁻¹ more negative than
620 the mean of the total dataset. The statistics of the expanded clusters of \mathbf{XS}_8 are much closer
621 to the total dataset. Notwithstanding, the largest magnitude differences between any frame
622 selection scheme and mean values of the 250 QM-cluster models are 0.62 kcal mol⁻¹ for ΔG^\ddagger
623 and 1.56 kcal mol⁻¹ for ΔG_{rxn} . For the expanded schemes, the largest absolute differences
624 decrease to 0.17 kcal mol⁻¹ for mean ΔG^\ddagger and 0.78 kcal mol⁻¹ for mean ΔG_{rxn} .

625 In summary, efforts to find a subset of MD frame selection schemes that best reflect
626 the kinetic and thermodynamic values of a large statistical ensemble were inconclusive, yet
627 promising. All eight schemes shown in Table 1, with 20 - 40 MD frames in each refined
628 to QM-cluster models, give reasonable approximations to the larger set of 250 MD frames.
629 Expanded schemes with 69 - 186 selected MD frames give mean values even closer to the
630 larger data set. Schemes employing k-means clustering to partition frames via structural
631 metrics did not perform better than schemes with completely random selected MD frames.
632 However, the QM-cluster models were built from one of three trimeric BsCM active sites (the
633 Chain A/C interface) that exhibited the least conformational fluctuation during the course
634 of the 20 ns MD simulation. Machine-learned selection procedures like k-means clustering
635 may be more beneficial for enzymes with more disordered regions or that undergo substantial
636 conformational changes during the simulation time.

637 Conclusions

638 Over 50 QM-cluster models of *Bacillus subtilis* chorismate mutase based on the X-ray crys-
639 tal structure, and an additional 250 QM-cluster models obtained from sampling MD frames
640 were extensively tested with the *RINRUS* software package being developed by our group.
641 *RINRUS* automatically identifies and trims fragments that interact with a substrate, allow-
642 ing quantitative and reproducible analysis of how the active site fragments affect enzyme
643 catalysis.

644 The smallest QM-cluster models built with *probe*, *arpeggio* and F-SAPT schemes showed
645 critical differences in how the kinetic and thermodynamics were altered by subsequent addi-
646 tion of residues. Once model building schemes approach the size of the “maximal” model,
647 all three iterative schemes behaved similarly. We have seen some methodological issues with
648 the *arpeggio* ranking scheme where ties can occur in the number of contact counts or con-
649 tact types. The tie issue in *arpeggio* was resolved manually, and fixed an outlying reaction
650 free energy that was observed in one of the smaller QM-cluster models. The solution to tie
651 interaction counts or types will require more automation to be incorporated into *RINRUS*
652 functionality.

653 The F-SAPT-based interaction energies highlight the importance of active site charged
654 residues. We recommend always using absolute values of F-SAPT interaction energies to
655 rank active site fragments in QM-cluster model construction. Rankings via signed inter-
656 action energies may de-prioritize important active site fragments that exhibit electrostatic
657 repulsion with a substrate. The unsigned F-SAPT ranking scheme showed slight improve-
658 ment of convergence compared to *probe* and *arpeggio* schemes, but no truncated models in
659 any of the schemes converged to within 1 kcal mol⁻¹ of the respective maximal models. We
660 again validate that there is no correlation between the number of *probe* contact counts and
661 E_{int} obtained from F-SAPT computations. More case studies are required to determine
662 if the small performance differences between schemes is related to the compact size of the
663 BsCM active site. Nevertheless, *probe*-based models, *arpeggio* and F-SAPT maximal models

664 are similar, providing evidence that the largest *RINRUS*-generated QM-cluster models are
665 robust and reliable.

666 As is widely known in the community and seen in our previous studies, B3LYP-GD3BJ
667 with small Pople-style basis sets and implicit solvation with CPCM systematically underes-
668 timates the free energies of activation of enzyme mechanisms compared to the experimental
669 kinetic value. A focus on the quality of the quantum chemical level of theory is purposefully
670 avoided in this work, to instead efficiently provide insight about QM-cluster model building
671 approaches.

672 The crystallographic protein structure was then solvated within an explicit water bath
673 and, over a 20 ns equilibrated MD simulation, 250 frames were selected to construct 250 QM-
674 cluster models of the active site. The proposed catalyzed Claisen rearrangement mechanism
675 was computed for all QM-cluster 250 models, and the reaction thermodynamics are observed
676 to fluctuate, with the activation free energy spanning 10.34 ± 2.62 kcal mol⁻¹ and the reaction
677 free energy spanning -15.38 ± 3.40 kcal mol⁻¹. The variation is shown to be primarily
678 due to the changes in residue/solvent/ligand positioning and conformation that occur over
679 the MD simulation, rather than differences in residue composition among the models. For
680 example, we noted that some active site residues highly ranked in the *probe*, *arpeggio*, and
681 F-SAPT schemes can be absent from specific MD frames when the residues shift to different
682 placements, but the computed kinetic and thermodynamic properties of those complexes
683 can still be reasonable given the QM-cluster model is suitably constructed. Furthermore,
684 while the catalytic mechanism is largely derived from charge stabilization interactions, and
685 we thus might expect the QM-cluster models to be very sensitive to changes in net model
686 charge. The results show most of the variation in ΔG^\ddagger and ΔG_{rxn} values is largely among
687 models with neutral net charge and a general insensitivity in predicted values with net charge
688 between ± 1 was observed. The active site interface with bulk solvent is shown to influence
689 kinetics and thermodynamics of the QM-cluster models. However, the number of explicit
690 water molecules included in the models appear to be inconsequential.

691 Collectively, results from the MD to QM-cluster model refinement point to the changing
692 molecular positioning rather than model composition as the main source for changing reac-
693 tion thermodynamics over the sampled times. We attempted to trace the thermodynamic
694 differences to simple, easily quantifiable structural differences among the models, specifically
695 by grouping models based upon RMSDs in backbone or side chain atoms. Ultimately, none of
696 the metrics were better than random selection for acceptably sampling a statistical ensemble
697 of structures. A more multifaceted technique will be required to efficiently cluster MD frames
698 for QM-cluster model refinement, especially if the enzyme undergoes major conformational
699 changes during the MD simulation.

700 This study exemplifies diverse features of the *RINRUS* toolkit by comparing the struc-
701 tural variation between X-ray crystal structure-based models and MD-based models of bacte-
702 rial chorismate mutase. Composition of QM-cluster models, or the QM region of a QM/MM
703 model is an essential part of reliability and accuracy in computational enzymology. For
704 far too long, a lack of automated model building techniques and software has hampered
705 advancement of the field as well as the reproducibility of seminal work. Here, QM-cluster
706 modeling provided insight into the enzymatic activity of chorismate mutase by connecting
707 the model composition, the contribution of charged residues, the influence of explicit solvent
708 water molecules, and positioning and orientation of active site residues to the computed
709 kinetic and thermodynamic values. Accompanying data can be easily used to perform fur-
710 ther cheminformatic analysis or to calibrate accuracy with more reliable quantum chemistry
711 methodologies; *RINRUS* was designed with reproducibility as a core feature.

712 Acknowledgments

713 This work is supported by the National Science Foundation (NSF) CAREER BIO-1846408
714 (for NJD and DAA), the Department of Energy (DOE) BES SBIR DE-SC0021568 (for NJD),
715 the National Institute of General Medical Sciences of the National Institutes of Health under

award number 1R35GM145206-01 (for QC), and the NSF Graduate Research Fellowship Program under Grant No. 1451514 (for TJS). The authors are grateful for the support provided by the University of Memphis High Performance Computing Center.

Author Contributions

Donatus A. Agbaglo: Conceptualization (equal); Formal analysis (lead); Investigation (lead); Methodology (equal); Visualization (lead); Writing – original draft (lead); Writing – review & editing (equal). **Thomas J. Summers:** Conceptualization (equal); Formal analysis (supporting); Methodology (equal); Visualization (supporting); Writing – original draft (supporting); Writing – review & editing (equal). **Qianyi Cheng:** Writing – review & editing (equal); Investigation (supporting). **Nathan J. DeYonker:** Conceptualization (equal); Resources (lead); Writing – original draft (supporting); Writing – review & editing (equal).

References

- (1) Kraut, D. A.; Carroll, K. S.; Herschlag, D. Challenges in enzyme mechanism and energetics. *Annu. Rev. Biochem.* **2003**, *72*, 517–571.
- (2) Cheng, Q.; DeYonker, N. J. Acylation and deacylation mechanism and kinetics of penicillin G reaction with *Streptomyces* R61 DD-peptidase. *J. Comput. Chem.* **2020**, *41*, 1685–1697.
- (3) Cheng, Q.; DeYonker, N. J. QM-Cluster Model Study of the Guaiacol Hydrogen Atom Transfer and Oxygen Rebound with Cytochrome P450 Enzyme GcoA. *J. Phys. Chem. B* **2021**, *125*, 3296–3306.
- (4) Summers, T. J.; Cheng, Q.; Palma, M. A.; Pham, D.-T.; Kelso III, D. K.; Web-

- 738 ster, C. E.; DeYonker, N. J. Cheminformatic quantum mechanical enzyme model design:
739 A catechol-O-methyltransferase case study. *Biophys. J.* **2021**, *120*, 3577–3587.
- 740 (5) Woodcock, H. L.; Hodošček, M.; Sherwood, P.; Lee, Y. S.; Schaefer III, H. F.;
741 Brooks, B. R. Exploring the quantum mechanical/molecular mechanical replica path
742 method: a pathway optimization of the chorismate to prephenate Claisen rearrange-
743 ment catalyzed by chorismate mutase. *Theor. Chem. Acc.* **2003**, *109*, 140–148.
- 744 (6) Lee, Y. S.; Worthington, S. E.; Krauss, M.; Brooks, B. R. Reaction mechanism of choris-
745 mate mutase studied by the combined potentials of quantum mechanics and molecular
746 mechanics. *J. Phys. Chem. B* **2002**, *106*, 12059–12065.
- 747 (7) Wiest, O.; Houk, K. On the transition state of the chorismate-prephenate rearrange-
748 ment. *J. Org. Chem.* **1994**, *59*, 7582–7584.
- 749 (8) Wiest, O.; Houk, K. Stabilization of the transition state of the chorismate-prephenate
750 rearrangement: An ab initio study of enzyme and antibody catalysis. *J. Am. Chem.*
751 *Soc.* **1995**, *117*, 11628–11639.
- 752 (9) Lyne, P. D.; Mulholland, A. J.; Richards, W. G. Insights into chorismate mutase catal-
753 ysis from a combined QM/MM simulation of the enzyme reaction. *J. Am. Chem. Soc.*
754 **1995**, *117*, 11345–11350.
- 755 (10) Davidson, M.; Guest, J.; Simon Craw, J.; Hillier, I.; Vincent, M. Conformational and
756 solvation aspects of the chorismate–prephenate rearrangement studied by *ab initio* elec-
757 tronic structure and simulation methods. *J. Chem. Soc., Perkin Trans. 2* **1997**, 1395–
758 1400.
- 759 (11) Hall, R. J.; Hindle, S. A.; Burton, N. A.; Hillier, I. H. Aspects of hybrid QM/MM
760 calculations: the treatment of the QM/MM interface region and geometry optimization
761 with an application to chorismate mutase. *J. Comput. Chem.* **2000**, *21*, 1433–1441.

- 762 (12) Khanjin, N. A.; Snyder, J. P.; Menger, F. Mechanism of chorismate mutase: Contri-
763 bution of conformational restriction to catalysis in the Claisen rearrangement. *J. Am.*
764 *Chem. Soc.* **1999**, *121*, 11831–11846.
- 765 (13) Madurga, S.; Vilaseca, E. SCRF study of the conformational equilibrium of chorismate
766 in water. *Phys. Chem. Chem. Phys.* **2001**, *3*, 3548–3554.
- 767 (14) Crespo, A.; Scherlis, D. A.; Martí, M. A.; Ordejón, P.; Roitberg, A. E.; Estrin, D. A. A
768 DFT-based QM-MM approach designed for the treatment of large molecular systems:
769 Application to chorismate mutase. *J. Phys. Chem. B* **2003**, *107*, 13728–13736.
- 770 (15) Dewick, P. M. The biosynthesis of shikimate metabolites. *Nat. Prod. Rep.* **1995**, *12*,
771 101–133.
- 772 (16) Andrews, P.; Smith, G. D.; Young, I. Transition-state stabilization and enzymic cataly-
773 sis. Kinetic and molecular orbital studies of the rearrangement of chorismate to prephen-
774 ate. *Biochem.* **1973**, *12*, 3492–3498.
- 775 (17) Gorisch, H. Mechanism of chorismate mutase reaction. *Biochem.* **1978**, *17*, 3700–3705.
- 776 (18) Freindorf, M.; Tao, Y.; Sethio, D.; Cremer, D.; Kraka, E. New mechanistic insights into
777 the Claisen rearrangement of chorismate—a Unified Reaction Valley Approach study.
778 *Mol. Phys.* **2019**, *117*, 1172–1192.
- 779 (19) Chook, Y. M.; Ke, H.; Lipscomb, W. N. Crystal structures of the monofunctional
780 chorismate mutase from *Bacillus subtilis* and its complex with a transition state analog.
781 *Proc. Natl. Acad. Sci. USA* **1993**, *90*, 8600–8603.
- 782 (20) Bruice, T. C. A view at the millennium: the efficiency of enzymatic catalysis. *Acc.*
783 *Chem. Res.* **2002**, *35*, 139–148.
- 784 (21) Claeysens, F.; Ranaghan, K. E.; Lawan, N.; Macrae, S. J.; Manby, F. R.; Harvey, J. N.;
785 Mulholland, A. J. Analysis of chorismate mutase catalysis by QM/MM modelling of

- 786 enzyme-catalysed and uncatalysed reactions. *Org. & Biomol. Chem.* **2011**, *9*, 1578–
787 1590.
- 788 (22) Burschowsky, D.; van Eerde, A.; Ökvist, M.; Kienhöfer, A.; Kast, P.; Hilvert, D.; Kren-
789 gel, U. Electrostatic transition state stabilization rather than reactant destabilization
790 provides the chemical basis for efficient chorismate mutase catalysis. *Proc. Natl. Acad.*
791 *Sci.* **2014**, *111*, 17516–17521.
- 792 (23) Zhang, X.; Zhang, X.; Bruice, T. C. A definitive mechanism for chorismate mutase.
793 *Biochem.* **2005**, *44*, 10443–10448.
- 794 (24) Lamb, A. L. Pericyclic reactions catalyzed by chorismate-utilizing enzymes. *Biochem.*
795 **2011**, *50*, 7476–7483.
- 796 (25) Štrajbl, M.; Shurki, A.; Kato, M.; Warshel, A. Apparent NAC effect in chorismate
797 mutase reflects electrostatic transition state stabilization. *J. Am. Chem. Soc.* **2003**,
798 *125*, 10228–10237.
- 799 (26) Galopin, C. C.; Zhang, S.; Wilson, D. B.; Ganem, B. On the mechanism of chorismate
800 mutases: clues from wild-type *E. coli* enzyme and a site-directed mutant related to
801 yeast chorismate mutase. *Tetrahedron Lett.* **1996**, *37*, 8675–8678.
- 802 (27) Liu, D. R.; Cload, S. T.; Pastor, R. M.; Schultz, P. G. Analysis of active site residues
803 in *Escherichia coli* chorismate mutase by site-directed mutagenesis. *J. Am. Chem. Soc.*
804 **1996**, *118*, 1789–1790.
- 805 (28) Zhang, S.; Kongsaree, P.; Clardy, J.; Wilson, D. B.; Ganem, B. Site-directed muta-
806 genesis of monofunctional chorismate mutase engineered from the *E. coli* P-protein.
807 *Bioorg. Med. Chem.* **1996**, *4*, 1015–1020.
- 808 (29) Schnappauf, G.; Sträter, N.; Lipscomb, W. N.; Braus, G. H. A glutamate residue in

- 809 the catalytic center of the yeast chorismate mutase restricts enzyme activity to acidic
810 conditions. *Proc. Natl. Acad. Sci. USA* **1997**, *94*, 8491–8496.
- 811 (30) Lassila, J. K.; Keeffe, J. R.; Kast, P.; Mayo, S. L. Exhaustive mutagenesis of six sec-
812 ondary active-site residues in *Escherichia coli* chorismate mutase shows the importance
813 of hydrophobic side chains and a helix N-capping position for stability and catalysis.
814 *Biochem.* **2007**, *46*, 6883–6891.
- 815 (31) Kienhöfer, A.; Kast, P.; Hilvert, D. Selective stabilization of the chorismate mutase
816 transition state by a positively charged hydrogen bond donor. *J. Am. Chem. Soc.* **2003**,
817 *125*, 3206–3207.
- 818 (32) Hur, S.; Bruice, T. C. Enzymes do what is expected (chalcone isomerase versus choris-
819 mate mutase). *J. Am. Chem. Soc.* **2003**, *125*, 1472–1473.
- 820 (33) Zhang, X.; Bruice, T. C. The proficiency of a thermophilic chorismate mutase enzyme
821 is solely through an entropic advantage in the enzyme reaction. *Proc. Natl. Acad. Sci.*
822 **2005**, *102*, 18356–18360.
- 823 (34) Shurki, A.; Štrajbl, M.; Villa, J.; Warshel, A. How much do enzymes really gain by
824 restraining their reacting fragments? *J. Am. Chem. Soc.* **2002**, *124*, 4097–4107.
- 825 (35) Burschowsky, D.; Krengel, U.; Uggerud, E.; Balcells, D. Quantum chemical modeling of
826 the reaction path of chorismate mutase based on the experimental substrate/product
827 complex. *FEBS. Open Bio.* **2017**, *7*, 789–797.
- 828 (36) Mulholland, A. J. Computational enzymology: modelling the mechanisms of biological
829 catalysts. 2008.
- 830 (37) Ahmadi, S.; Barrios Herrera, L.; Chehelamirani, M.; Hostaš, J.; Jalife, S.;
831 Salahub, D. R. Multiscale modeling of enzymes: QM-cluster, QM/MM, and
832 QM/MM/MD: A tutorial review. *Intl. J. Quant. Chem.* **2018**, *118*, e25558.

- 833 (38) Guo, H.; Rao, N. Chorismate-Mutase-Catalyzed Claisen Rearrangement. *The Claisen*
834 *Rearrangement: Methods and Applications* **2007**, 1–23.
- 835 (39) Kulik, H. J.; Zhang, J.; Klinman, J. P.; Martínez, T. J. How large should the QM
836 region be in QM/MM calculations? The case of catechol O-methyltransferase. *J. Phys.*
837 *Chem. B* **2016**, *120*, 11381–11394.
- 838 (40) Kulik, H. J.; Luehr, N.; Ufimtsev, I. S.; Martinez, T. J. Ab initio quantum chemistry
839 for protein structures. *J. Phys. Chem. B* **2012**, *116*, 12501–12509.
- 840 (41) Karelina, M.; Kulik, H. J. Systematic quantum mechanical region determination in
841 QM/MM simulation. *J. Chem. Theory Comput.* **2017**, *13*, 563–576.
- 842 (42) Sumner, S.; Soderhjelm, P.; Ryde, U. Effect of geometry optimizations on QM-cluster
843 and QM/MM studies of reaction energies in proteins. *J. Chem. Theory Comput.* **2013**,
844 *9*, 4205–4214.
- 845 (43) Hu, L.; Eliasson, J.; Heimdal, J.; Ryde, U. Do quantum mechanical energies calculated
846 for small models of protein-active sites converge? *J. Phys. Chem. A* **2009**, *113*, 11793–
847 11800.
- 848 (44) Delcey, M. G.; Pierloot, K.; Phung, Q. M.; Vancoillie, S.; Lindh, R.; Ryde, U. Accurate
849 calculations of geometries and singlet–triplet energy differences for active-site models
850 of [NiFe] hydrogenase. *Phys. Chem. Chem. Phys.* **2014**, *16*, 7927–7938.
- 851 (45) Wappett, D. A.; Goerigk, L. A guide to benchmarking enzymatically catalysed reac-
852 tions: the importance of accurate reference energies and the chemical environment.
853 *Theor. Chem. Acc.* **2021**, *140*, 1–15.
- 854 (46) Kromann, J. C.; Christensen, A. S.; Cui, Q.; Jensen, J. H. Towards a barrier height
855 benchmark set for biologically relevant systems. *PeerJ* **2016**, *4*, e1994.

- 856 (47) Di Paola, L.; De Ruvo, M.; Paci, P.; Santoni, D.; Giuliani, A. Protein contact networks:
857 an emerging paradigm in chemistry. *Chem. Rev.* **2013**, *113*, 1598–1613.
- 858 (48) Doncheva, N. T.; Klein, K.; Domingues, F. S.; Albrecht, M. Analyzing and visualizing
859 residue networks of protein structures. *Trends Biochem. Sci.* **2011**, *36*, 179–182.
- 860 (49) Deng, Z.; Chuaqui, C.; Singh, J. Structural interaction fingerprint (SIFt): a novel
861 method for analyzing three-dimensional protein-ligand binding interactions. *J. Med.*
862 *Chem.* **2004**, *47*, 337–344.
- 863 (50) Szalewicz, K. Symmetry-adapted perturbation theory of intermolecular forces. *Wiley*
864 *Interdiscip. Rev. Comput. Mol. Sci.* **2012**, *2*, 254–272.
- 865 (51) Parker, T. M.; Burns, L. A.; Parrish, R. M.; Ryno, A. G.; Sherrill, C. D. Levels of
866 symmetry adapted perturbation theory (SAPT). I. Efficiency and performance for in-
867 teraction energies. *J. Chem. Phys.* **2014**, *140*, 094106.
- 868 (52) Parrish, R. M.; Parker, T. M.; Sherrill, C. D. Chemical assignment of symmetry-adapted
869 perturbation theory interaction energy components: the functional-group SAPT parti-
870 tion. *J. Chem. Theory Comput.* **2014**, *10*, 4417–4431.
- 871 (53) Parrish, R. M.; Thompson, K. C.; Martinez, T. J. Large-scale functional group
872 symmetry-adapted perturbation theory on graphical processing units. *J. Chem. Theory*
873 *Comput.* **2018**, *14*, 1737–1753.
- 874 (54) Heilmann, N.; Wolf, M.; Kozłowska, M.; Sedghamiz, E.; Setzler, J.; Brieg, M.; Wen-
875 zel, W. Sampling of the conformational landscape of small proteins with Monte Carlo
876 methods. *Sci. Rep.* **2020**, *10*, 1–13.
- 877 (55) Word, J. M.; Lovell, S. C.; Richardson, J. S.; Richardson, D. C. Asparagine and glu-
878 tamine: using hydrogen atom contacts in the choice of side-chain amide orientation. *J.*
879 *Mol. Biol.* **1999**, *285*, 1735–1747.

- 880 (56) Word, J. M.; Lovell, S. C.; LaBean, T. H.; Taylor, H. C.; Zalis, M. E.; Presley, B. K.;
881 Richardson, J. S.; Richardson, D. C. Visualizing and quantifying molecular goodness-
882 of-fit: small-probe contact dots with explicit hydrogen atoms. *J. Mol. Biol.* **1999**, *285*,
883 1711–1733.
- 884 (57) Jubb, H. C.; Higuero, A. P.; Ochoa-Montaña, B.; Pitt, W. R.; Ascher, D. B.; Blun-
885 dell, T. L. Arpeggio: a web server for calculating and visualising interatomic interactions
886 in protein structures. *J. Mol. Biol.* **2017**, *429*, 365–371.
- 887 (58) Cheng, Q.; DeYonker, N. J.; Summers, T. J.; Agbaglo, D. A.; Suhagia, T.; Palma, M. A.
888 GitHub - natedey/RINRUS: Residue Interaction Network Residue Selector (RINRUS)
889 public release. <https://github.com/natedey/RINRUS> (accessed 2022-09-14). 2022.
- 890 (59) Schreyer, A.; Blundell, T. CREDO: a protein–ligand interaction database for drug
891 discovery. *Chem. Biol. Drug Des.* **2009**, *73*, 157–167.
- 892 (60) Hehre, W. J.; Ditchfield, R.; Pople, J. A. Self-consistent molecular orbital methods.
893 XII. Further extensions of Gaussian-type basis sets for use in molecular orbital studies
894 of organic molecules. *J. Chem. Phys.* **1972**, *56*, 2257–2261.
- 895 (61) Misquitta, A. J.; Podeszwa, R.; Jeziorski, B.; Szalewicz, K. Intermolecular potentials
896 based on symmetry-adapted perturbation theory with dispersion energies from time-
897 dependent density-functional calculations. *J. Chem. Phys.* **2005**, *123*, 214103.
- 898 (62) Bukowski, R.; Cencek, W.; Jankowski, P.; Jeziorska, M.; Jeziorski, B.; Kucharski, S.;
899 Lotrich, V.; Misquitta, A.; Moszynski, R.; Patkowski, K., et al. SAPT2008: An *ab*
900 *initio* program for many-body symmetry-adapted perturbation theory calculations of
901 intermolecular interaction energies. *University of Delaware and University of Warsaw*
902 **2008**,
- 903 (63) Spronk, S. A.; Glick, Z. L.; Metcalf, D. P.; Sherrill, C. D.; Cheney, D. L. A quantum

- 904 chemical interaction energy dataset for accurately modeling protein-ligand interactions.
905 *Sci. Data* **2023**, *10*, 619.
- 906 (64) Parrish, R. M.; Burns, L. A.; Smith, D. G.; Simmonett, A. C.; DePrince III, A. E.;
907 Hohenstein, E. G.; Bozkaya, U.; Sokolov, A. Y.; Di Remigio, R.; Richard, R. M.,
908 et al. Psi4 1.1: An open-source electronic structure program emphasizing automation,
909 advanced libraries, and interoperability. *J. Chem. Theory Comput.* **2017**, *13*, 3185–
910 3197.
- 911 (65) Burns, L. A.; Faver, J. C.; Zheng, Z.; Marshall, M. S.; Smith, D. G.; Vanommes-
912 laeghe, K.; MacKerell Jr, A. D.; Merz Jr, K. M.; Sherrill, C. D. The BioFragment
913 Database (BFDb): An open-data platform for computational chemistry analysis of
914 noncovalent interactions. *J. Chem. Phys.* **2017**, *147*, 161727.
- 915 (66) Summers, T. J.; Daniel, B. P.; Cheng, Q.; DeYonker, N. J. Quantifying Inter-Residue
916 Contacts through Interaction Energies. *J. Chem. Inf. Model* **2019**, *59*, 5034–5044.
- 917 (67) Summers, T. J.; Hemmati, R.; Miller, J. E.; Agbaglo, D. A.; Cheng, Q.; DeYonker, N. J.
918 Evaluating the Active Site-Substrate Interplay Between X-ray Crystal Structure and
919 Molecular Dynamics in Chorismate Mutase. *J. Chem. Phys.* **2023**, *158*, 065101.
- 920 (68) Frisch, M.; Trucks, G.; Schlegel, H.; Scuseria, G.; Robb, M.; Cheeseman, J.; Scal-
921 mani, G.; Barone, V.; Petersson, G.; Nakatsuji, H., et al. Gaussian 16. 2016.
- 922 (69) Beck, A. D. Density-functional thermochemistry. III. The role of exact exchange. *J.*
923 *Chem. Phys.* **1993**, *98*, 5648–6.
- 924 (70) Lee, C.; Yang, W.; Parr, R. G. Development of the Colle-Salvetti correlation-energy
925 formula into a functional of the electron density. *Phys. Rev. B* **1988**, *37*, 785.
- 926 (71) Petersson, G.; Al-Laham, M. A. A complete basis set model chemistry. II. Open-shell

- 927 systems and the total energies of the first-row atoms. *J. Chem. Phys.* **1991**, *94*, 6081–
928 6090.
- 929 (72) Grimme, S.; Ehrlich, S.; Goerigk, L. Effect of the damping function in dispersion cor-
930 rected density functional theory. *J. Comput. Chem.* **2011**, *32*, 1456–1465.
- 931 (73) Barone, V.; Cossi, M. Quantum calculation of molecular energies and energy gradients
932 in solution by a conductor solvent model. *J. Phys. Chem. A* **1998**, *102*, 1995–2001.
- 933 (74) Cossi, M.; Rega, N.; Scalmani, G.; Barone, V. Energies, structures, and electronic
934 properties of molecules in solution with the C-PCM solvation model. *J. Comput. Chem.*
935 **2003**, *24*, 669–681.
- 936 (75) Worthington, S. E.; Roitberg, A. E.; Krauss, M. An MD/QM study of the chorismate
937 mutase-catalyzed Claisen rearrangement reaction. *J. Phys. Chem. B* **2001**, *105*, 7087–
938 7095.
- 939 (76) Gordon, J. C.; Myers, J. B.; Folta, T.; Shoja, V.; Heath, L. S.; Onufriev, A. H++: a
940 server for estimating p K as and adding missing hydrogens to macromolecules. *Nucleic
941 Acids Res.* **2005**, *33*, W368–W371.
- 942 (77) Case, D.; Cerutti, D.; Cheatham, T.; Darden, T.; Duke, R.; Giese, T.; Gohlke, H.;
943 Goetz, A.; Greene, D.; Homeyer, N., et al. Amber18 (University of San Francisco).
944 **2017**,
- 945 (78) Wang, J.; Wolf, R. M.; Caldwell, J. W.; Kollman, P. A.; Case, D. A. Development and
946 testing of a general amber force field. *J. Comput. Chem.* **2004**, *25*, 1157–1174.
- 947 (79) Jorgensen, W. L.; Chandrasekhar, J.; Madura, J. D.; Impey, R. W.; Klein, M. L.
948 Comparison of simple potential functions for simulating liquid water. *J. Chem. Phys.*
949 **1983**, *79*, 926–935.

- 950 (80) Joung, I. S.; Cheatham III, T. E. Determination of alkali and halide monovalent ion
951 parameters for use in explicitly solvated biomolecular simulations. *J. Phys. Chem. B*
952 **2008**, *112*, 9020–9041.
- 953 (81) Andersen, H. C. Rattle: A “velocity” version of the shake algorithm for molecular
954 dynamics calculations. *J. Comput. Phys.* **1983**, *52*, 24–34.
- 955 (82) Roe, D. R.; Cheatham III, T. E. PTRAJ and CPPTRAJ: software for processing and
956 analysis of molecular dynamics trajectory data. *J. Chem. Theory Comput.* **2013**, *9*,
957 3084–3095.
- 958 (83) Ishida, T. Probing protein environment in an enzymatic process: All-electron quantum
959 chemical analysis combined with *ab initio* quantum mechanical/molecular mechanical
960 modeling of chorismate mutase. *J. Chem. Phys.* **2008**, *129*, 09B618.
- 961 (84) Ishida, T. Effects of point mutation on enzymatic activity: correlation between protein
962 electronic structure and motion in chorismate mutase reaction. *J. Am. Chem. Soc.*
963 **2010**, *132*, 7104–7118.
- 964 (85) Cheng, Q.; DeYonker, N. J. The Glycine N-Methyltransferase Case Study: Another
965 Challenge for QM-Cluster Models? *J. Phys. Chem. B* **2023**,
- 966 (86) Kast, P.; Asif-Ullah, M.; Hilvert, D. Is chorismate mutase a prototypic entropy trap?
967 - Activation parameters for the *Bacillus subtilis* enzyme. *Tetrahedron lett.* **1996**, *37*,
968 2691–2694.
- 969 (87) Wappett, D. A.; Goerigk, L. Toward a quantum-chemical benchmark set for enzymat-
970 ically catalyzed reactions: important steps and insights. *J. Phys. Chem. A* **2019**, *123*,
971 7057–7074.
- 972 (88) Goerigk, L.; Grimme, S. A thorough benchmark of density functional methods for gen-

- 973 eral main group thermochemistry, kinetics, and noncovalent interactions. *Phys. Chem.*
974 *Chem. Phys.* **2011**, *13*, 6670–6688.
- 975 (89) Jurečka, P.; Šponer, J.; Černý, J.; Hobza, P. Benchmark database of accurate (MP2
976 and CCSD (T) complete basis set limit) interaction energies of small model complexes,
977 DNA base pairs, and amino acid pairs. *Phys. Chem. Chem. Phys.* **2006**, *8*, 1985–1993.
- 978 (90) Antony, J.; Grimme, S. Density functional theory including dispersion corrections for
979 intermolecular interactions in a large benchmark set of biologically relevant molecules.
980 *Phys. Chem. Chem. Phys.* **2006**, *8*, 5287–5293.
- 981 (91) Kesharwani, M. K.; Karton, A.; Martin, J. M. Benchmark *ab initio* conformational
982 energies for the proteinogenic amino acids through explicitly correlated methods. As-
983 sessment of density functional methods. *J. Chem. Theory Comput.* **2016**, *12*, 444–454.
- 984 (92) Paiva, P.; Ramos, M. J.; Fernandes, P. A. Assessing the validity of DLPNO-CCSD (T)
985 in the calculation of activation and reaction energies of ubiquitous enzymatic reactions.
986 *J. Comput. Chem.* **2020**, *41*, 2459–2468.
- 987 (93) Ribeiro, A. J.; Santos-Martins, D.; Russo, N.; Ramos, M. J.; Fernandes, P. A. Enzy-
988 matic flexibility and reaction rate: a QM/MM study of HIV-1 protease. *ACS Catal.*
989 **2015**, *5*, 5617–5626.
- 990 (94) Ryde, U. How many conformations need to be sampled to obtain converged QM/MM
991 energies? The curse of exponential averaging. *J. Chem. Theory Comput.* **2017**, *13*,
992 5745–5752.
- 993 (95) Dokainish, H.; Gault, J. Computational Approach Choice in Modeling Flexible Enzyme
994 Active Sites. **2019**,
- 995 (96) Mei, Z.; Treado, J. D.; Grigas, A. T.; Levine, Z. A.; Regan, L.; O’hern, C. S. Analyses

996 of protein cores reveal fundamental differences between solution and crystal structures.

997 *Proteins* **2020**, *88*, 1154–1161.

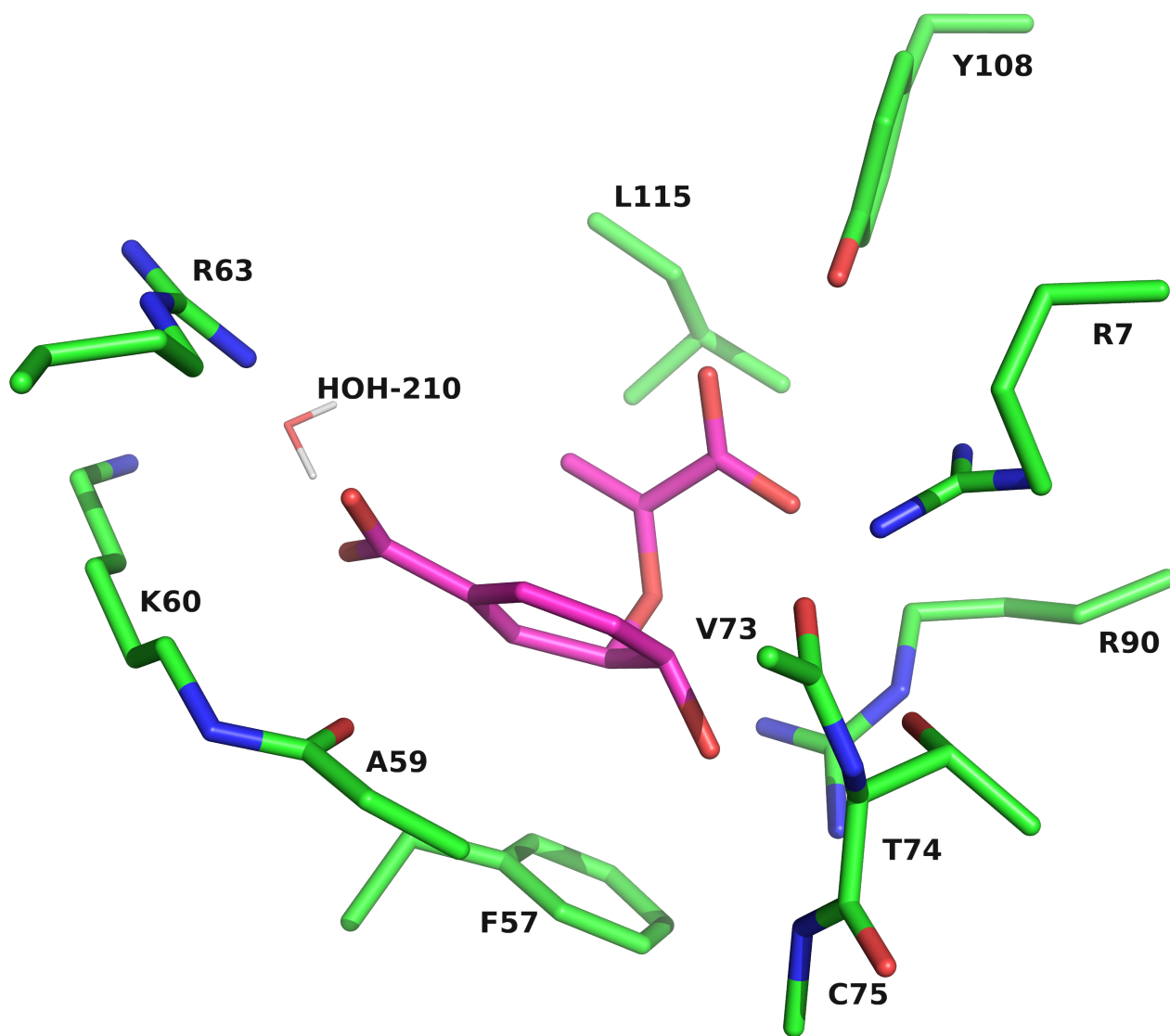


Figure 1: 3D representation of the *RINRUS* maximal model, from the X-ray crystal structure of *Bacillus subtilis* chorismate mutase, using the *probe* ranking scheme. Substrate carbon atoms are colored in magenta. Except for those of the crystallographically resolved water molecule, hydrogen atoms are omitted for clarity.

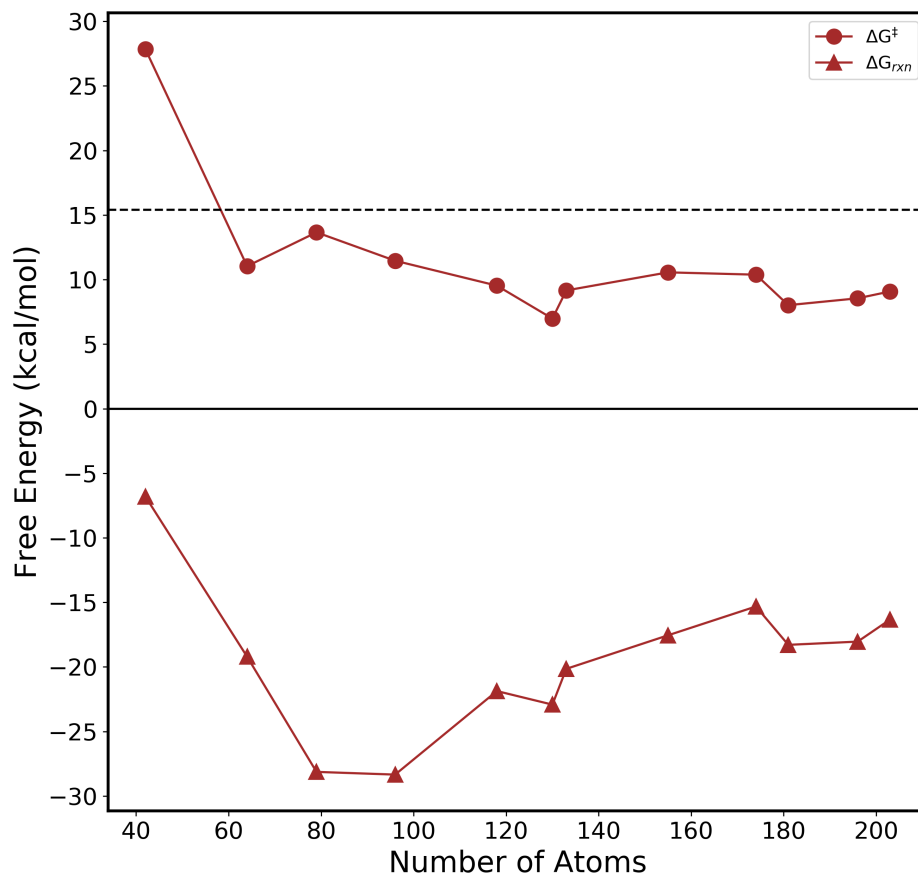


Figure 2: Kinetics and thermodynamics of the iteratively grown QM-cluster models using the *probe* ranking scheme. Computed ΔG^\ddagger values are represented by circles and ΔG_{rxn} values by triangles. The black dashed line shows the experimental ΔG^\ddagger value from reference.⁸⁶

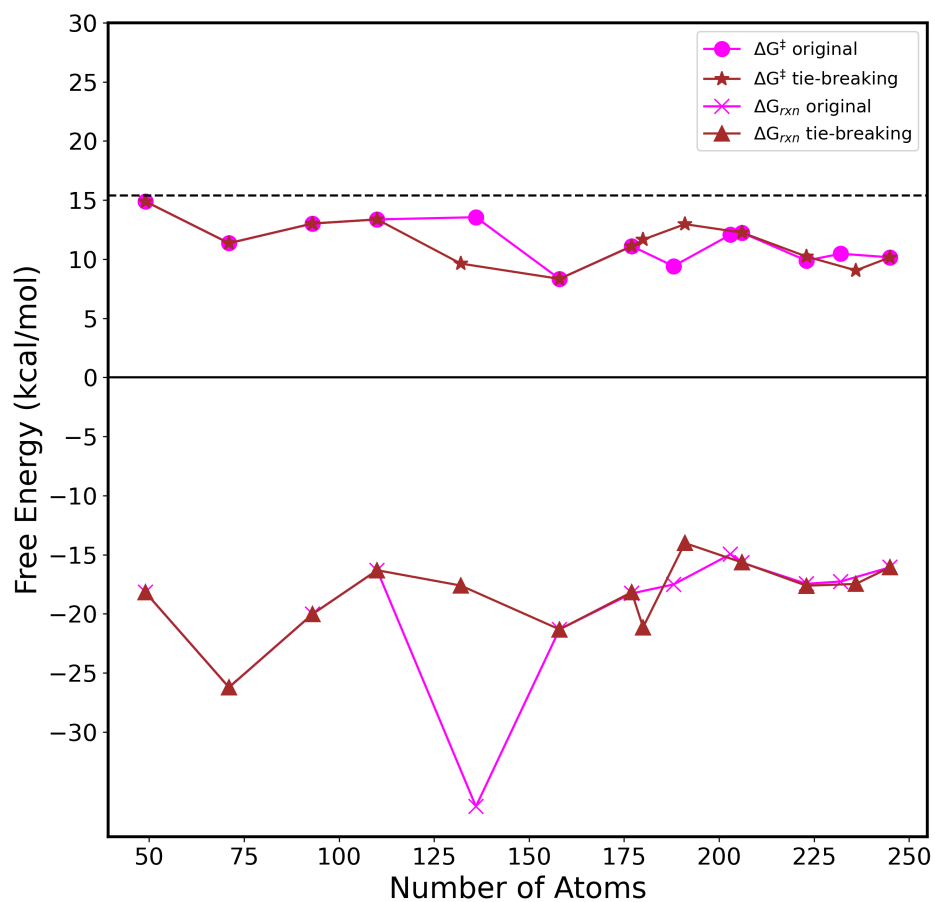


Figure 3: Kinetics and thermodynamics of the iteratively grown QM-cluster models using the *arpeggio* ranking scheme. Computed ΔG^\ddagger values are represented by circles and stars, and ΔG_{rxn} values by crosses and triangles. The original ranking is given in magenta, while values from the tie-breaking scheme are given in brown. The black dashed line shows the experimental ΔG^\ddagger value from reference.⁸⁶

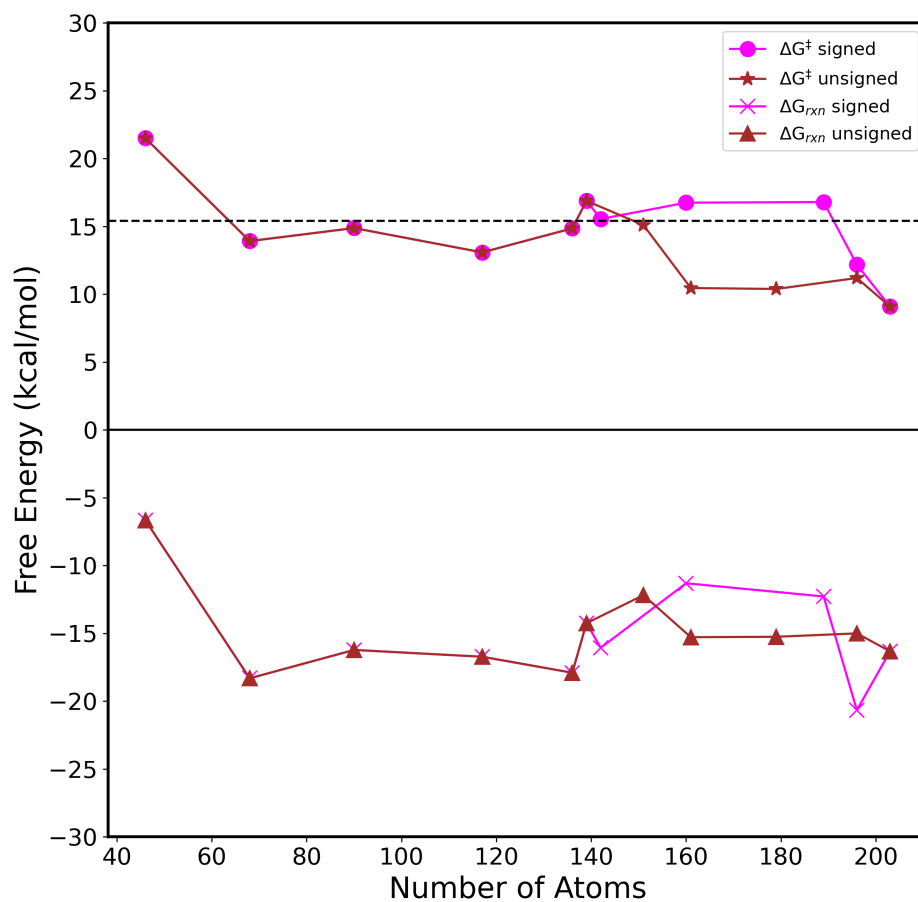


Figure 4: Kinetics and thermodynamics of the iteratively grown QM-cluster models using the F-SAPT ranking scheme. Computed ΔG^\ddagger values are represented by circles and stars, and ΔG_{rxn} values by crosses and triangles. The signed ranking order is given in magenta, while the unsigned ranking order is given in brown. The black dashed line shows the experimental ΔG^\ddagger value from reference.⁸⁶

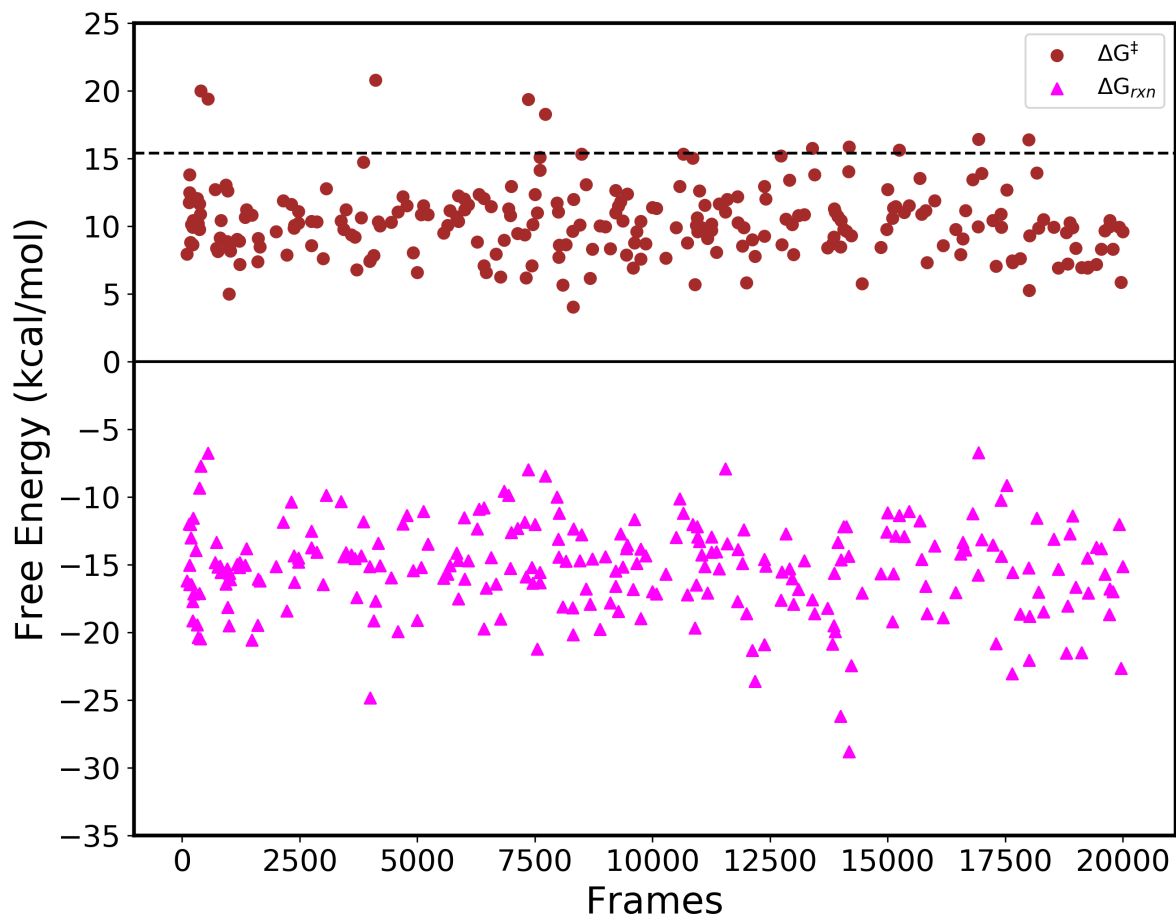


Figure 5: Computed values of ΔG^\ddagger (circle) and ΔG_{rxn} (triangle) for the 250 maximal QM-cluster models plotted against the select frame number (each representing a time scale of 1 ps). The black dashed line at the top is the experimental value from reference.⁸⁶

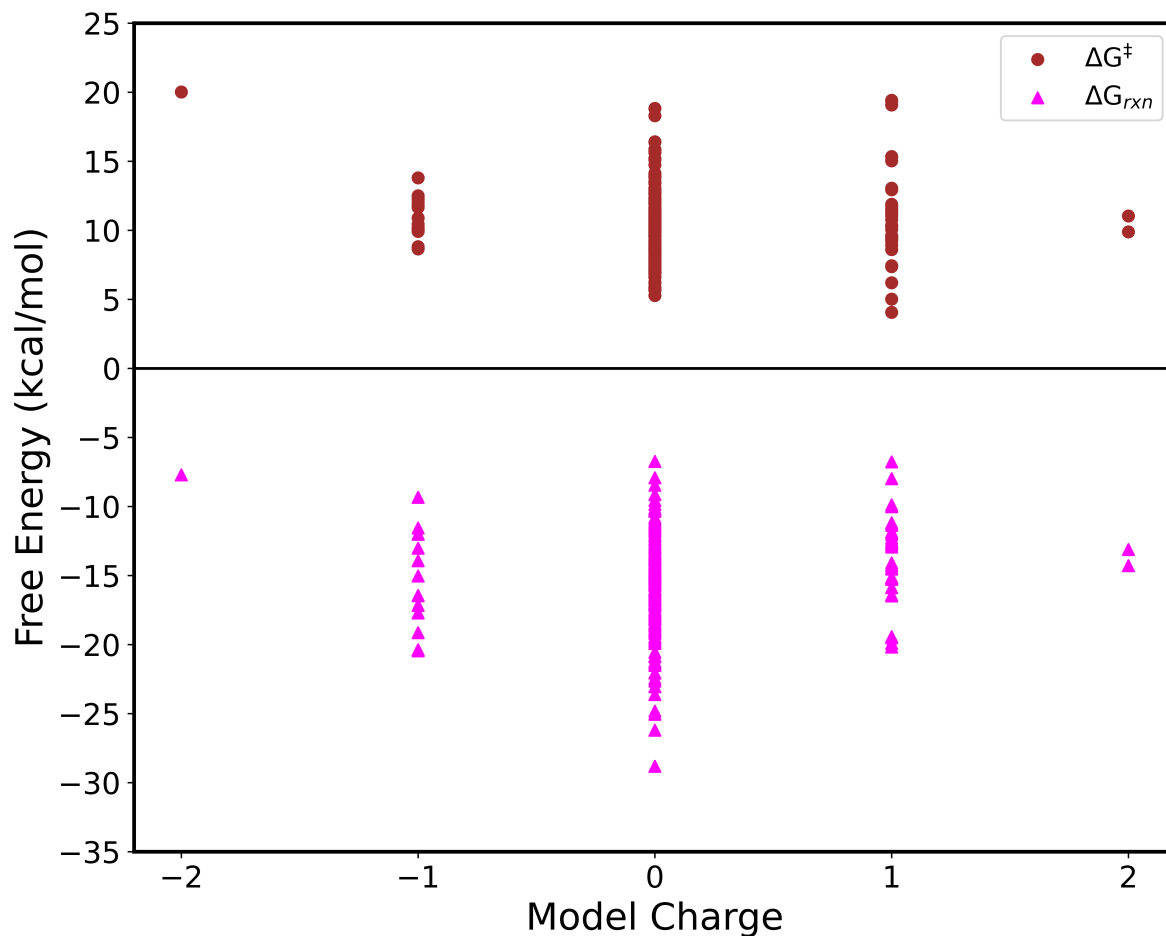


Figure 6: Charge distribution for the 250 QM-cluster models refined from MD frames. The corresponding number of QM-cluster models for each net model charge is: charge -2 = 1 QM-cluster model, charge -1 = 14 QM-cluster models, charge 0 = 200 QM-cluster models, charge +1 = 33 QM cluster models, and charge +2 = 2 QM-cluster models.

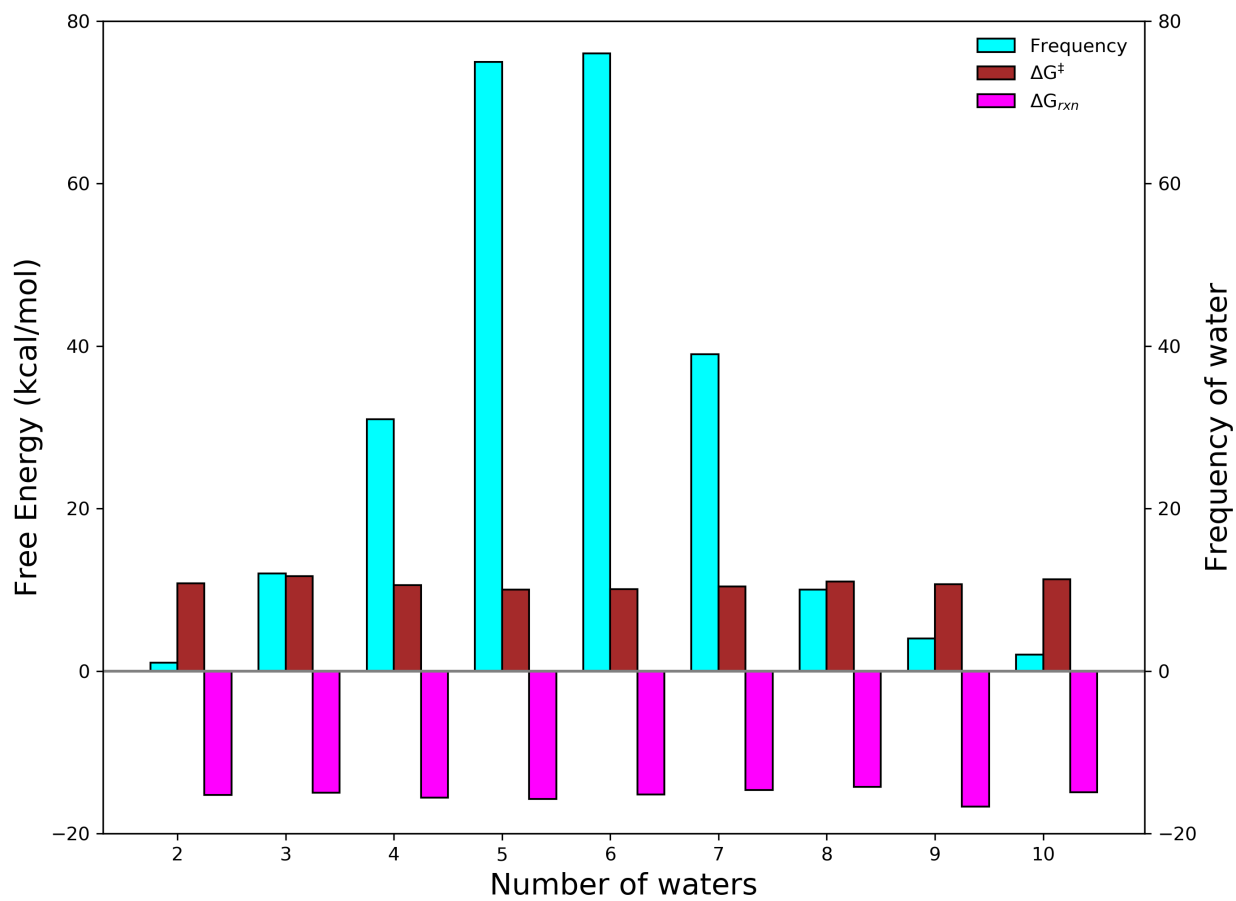


Figure 7: Mean activation free energy (brown), reaction free energy (magenta), and number of QM-cluster models with a given number of explicit water molecules (cyan) identified as having interatomic contacts with the chorismate for the 250 QM-cluster models built from selected MD frames.

Table 1: Mean free energies of activation and reaction for the various MD frame selection schemes. K-means clusters are labelled with a C (all in kcal mol⁻¹).

Scheme	Cluster	# of frames	ΔG^\ddagger	σ	ΔG_{rxn}	σ
S₁		20	10.07	± 2.87	-16.23	± 3.90
S₂		30	10.12	± 2.39	-16.28	± 3.82
S₃		30	10.03	± 2.83	-14.99	± 3.06
S₄		30	10.06	± 1.88	-15.92	± 2.86
S₅		30	10.29	± 3.05	-15.57	± 3.09
	C ₁	10	9.90	± 2.74	-16.78	± 3.12
	C ₂	10	11.03	± 3.98	-15.54	± 3.48
	C ₃	10	9.95	± 1.92	-14.40	± 2.02
S₆		40	10.23	± 2.38	-15.24	± 3.04
S₇		40	10.74	± 2.69	-15.35	± 3.52
S₈		30	10.96	± 2.69	-13.82	± 3.36
	C ₁	10	10.83	± 1.95	-13.85	± 2.30
	C ₂	10	10.80	± 3.94	-13.57	± 4.15
	C ₃	10	11.49	± 1.41	-14.06	± 3.34
Combined		250	10.34	± 2.62	-15.38	± 3.40

Table 2: Mean free energies of activation and reaction for the expanded schemes. The individual k-means clusters are labelled XC (all in kcal mol⁻¹).

Scheme	Cluster	# of frames	ΔG^\ddagger	σ	ΔG_{rxn}	σ
S₁+S₆+S₇		100	10.40	± 2.63	-15.48	± 3.44
XS₂		148	10.17	± 2.75	-15.64	± 3.44
XS₃		173	10.35	± 2.70	-15.46	± 3.50
XS₄		186	10.39	± 2.64	-15.36	± 3.37
XS₅						
	XC ₁	92	10.25	± 2.63	-16.16	± 3.92
	XC ₂	89	10.30	± 2.85	-15.00	± 3.05
	XC ₃	69	10.50	± 2.28	-14.85	± 2.83
XS₈						
	XC ₁	77	10.42	± 2.52	-15.38	± 3.54
	XC ₂	81	10.27	± 2.86	-15.05	± 3.39
	XC ₃	92	10.32	± 2.49	-15.69	± 3.24
Combined		250	10.34	± 2.62	-15.38	± 3.40